



# A monoastral mitotic spindle determines lineage fate and position in the mouse embryo

Oz Pomp<sup>1</sup>, Hui Yi Grace Lim<sup>2</sup>, Robin M. Skory<sup>1</sup>, Adam A. Moverley<sup>1</sup>, Piotr Tetlak<sup>1</sup>, Stephanie Bissiere<sup>1</sup> and Nicolas Plachta<sup>1</sup>  

**During mammalian development, the first asymmetric cell divisions segregate cells into inner and outer positions of the embryo to establish the pluripotent and trophectoderm lineages. Typically, polarity components differentially regulate the mitotic spindle via astral microtubule arrays to trigger asymmetric division patterns. However, early mouse embryos lack centrosomes, the microtubule-organizing centres (MTOCs) that usually generate microtubule asters. Thus, it remains unknown whether spindle organization regulates lineage segregation. Here we find that heterogeneities in cell polarity in the early 8-cell-stage mouse embryo trigger the assembly of a highly asymmetric spindle organization. This spindle arises in an unusual modular manner, forming a single microtubule aster from an apically localized, non-centrosomal MTOC, before joining it to the rest of the spindle apparatus. When fully assembled, this ‘monoastral’ spindle triggers spatially asymmetric division patterns to segregate cells into inner and outer positions. Moreover, the asymmetric inheritance of spindle components causes differential cell polarization to determine pluripotent versus trophectoderm lineage fate.**

Asymmetric cell divisions produce a wide diversity of cell lineages<sup>1</sup>. In the mouse embryo, the first lineage segregation occurs when 8-cell blastomeres divide and segregate daughters into the pluripotent inner cell mass and outer trophectoderm<sup>2</sup>. Some divisions directly separate cells into inner and outer positions. Others allocate both daughters to the outer region, but can be followed by internalization of one daughter via apical constriction, a process driven by cortical tension<sup>3</sup>. Following segregation, outer cells polarize their apical cortex<sup>4</sup>. They establish a cortical F-actin ring, which scaffolds apical polarity proteins such as Pard6b, Ezrin and keratins. This polarization triggers differential regulation of the transcriptional regulators Yap and Cdx2, which specifies trophectoderm over pluripotent fate<sup>5–8</sup>. Inner cells remain unpolarized and express pluripotency-associated factors. The mechanism determining inner–outer cell segregation and differential polarization is unknown<sup>9</sup>.

Some studies proposed that inner–outer segregation is stochastic and cannot be predicted by cell heterogeneities or cleavage patterns<sup>10–12</sup>. Yet, others found heterogeneities in the early embryo predicting inner–outer position, including differences in transcriptional regulation<sup>13–18</sup>. These heterogeneities could bias division patterns, but the mechanism remains elusive. In many polarized tissues, cortical proteins differentially regulate the mitotic spindle via astral microtubules to trigger asymmetric division patterns and lineage segregation<sup>19</sup>. However, mouse embryos do not inherit centrioles and are thought to lack centrosomes and astral microtubules until blastocyst stages<sup>20–23</sup>.

Other studies have proposed a model whereby the apical domain of 8-cell blastomeres orients the spindle along the apical–basal axis to bias division angles. Yet, these spindle alignments have not been visualized in intact embryos and it is unclear how the apical cortex could influence spindle alignments without asters<sup>12,24</sup>. It has also been proposed that the apical domain might be asymmetrically inherited during division to differentially regulate tension and cell position after division<sup>11</sup>. However, live-embryo imaging showed

that the apical domain disassembles before division and is not directly inherited<sup>25,26</sup>. Finally, keratin filaments are asymmetrically inherited by outer cells where they promote trophectoderm specification, yet it is unknown whether keratins interact with the mitotic spindle<sup>25</sup>. Therefore, the interplay between polarity, spindles and lineage segregation remains uncertain.

## Results

**An atypical mitotic spindle in the mouse embryo.** To investigate spindle organization, we used  $\alpha$ -tubulin immunofluorescence. At the 4- to 8-cell stage, spindles display few or no astral arrays (Fig. 1a), consistent with a lack of centrosomes<sup>22,23</sup>. Furthermore, the two halves of the metaphase spindle comprising kinetochore and non-kinetochore microtubules (that is, the inter-polar regions)<sup>27</sup> are symmetric in length and density (Fig. 1a). At blastocyst stage, spindles display more focused spindle poles, yet they also lack asters (Fig. 1a). Thus, we refer to these spindles as ‘anastral’<sup>22</sup>. During the 8- to 16-cell stage, cells also display anastral spindles. However, a subset of cells establishes an asymmetric organization displaying a prominent aster between the apical pole and cortex (Fig. 1b–d, Extended Data Fig. 1a,c and Supplementary Video 1). Thus, we investigated how these monoastral spindles arise.

## The monoastral spindle assembles in a modular manner.

Investigation of proteins supporting MTOCs suggested the involvement of PLK1<sup>28</sup>. Sister cells in mouse embryos remain connected by their cytokinetic bridge after division. This bridge accumulates PLK1 and functions as MTOC throughout interphase<sup>29</sup>. However, PLK1–Emerald disappears from the bridge at the end of interphase and accumulates in the nucleus before nuclear envelope breakdown (NEBD) (Extended Data Fig. 2a–e). We identified two additional PLK1–Emerald foci that appear before NEBD: one forms at the perinuclear region in all 8-cell blastomeres (Fig. 2a,g), while a subset of cells forms a second structure at the apical cortex (Fig. 2a;

<sup>1</sup>Department of Cell and Developmental Biology, Institute for Regenerative Medicine, Perelman School of Medicine, University of Pennsylvania, Philadelphia, PA, USA. <sup>2</sup>Institute of Molecular and Cell Biology, ASTAR, Singapore, Singapore. ✉e-mail: [nicolas.plachta@penncellbiology.upenn.edu](mailto:nicolas.plachta@penncellbiology.upenn.edu)

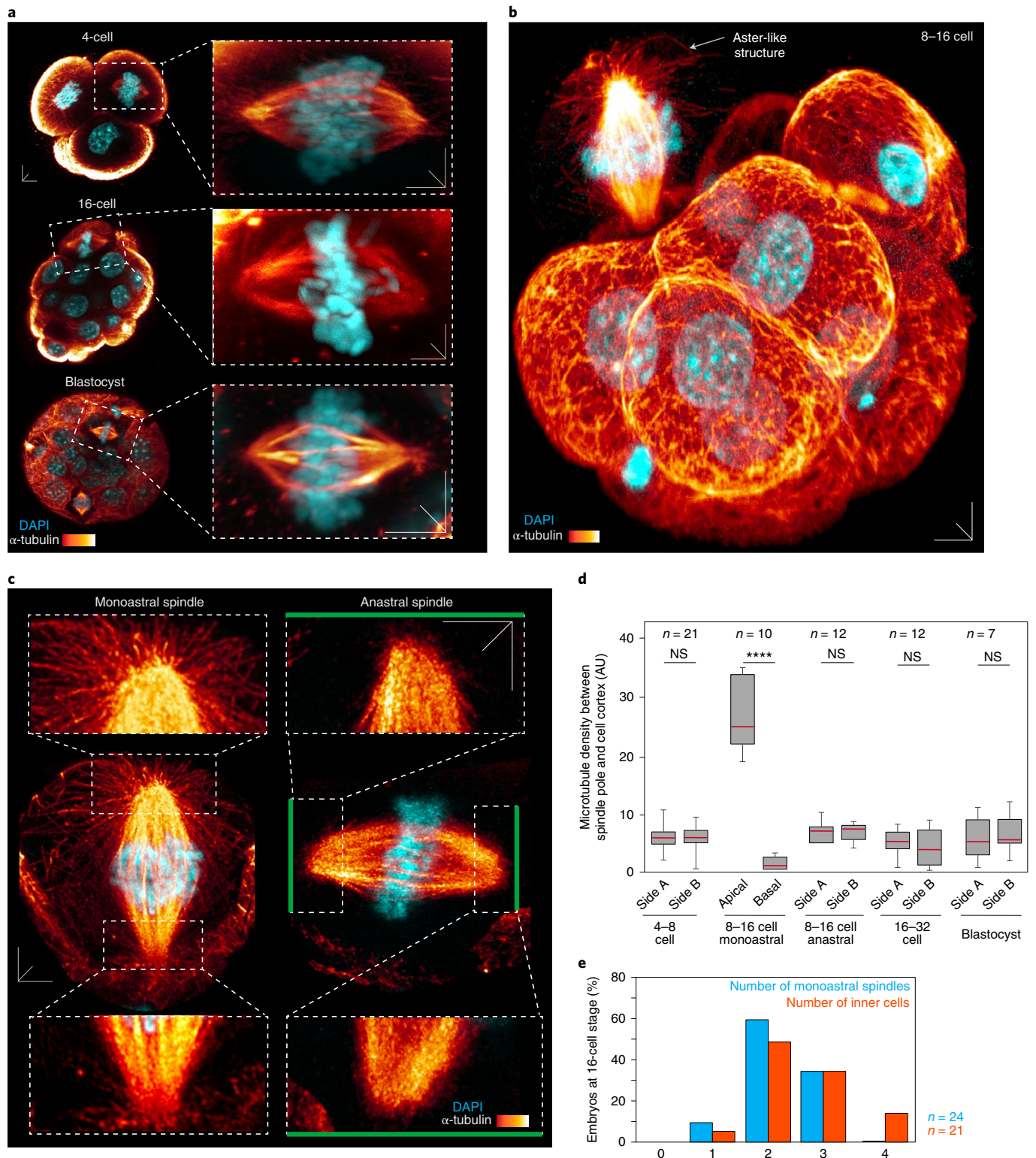
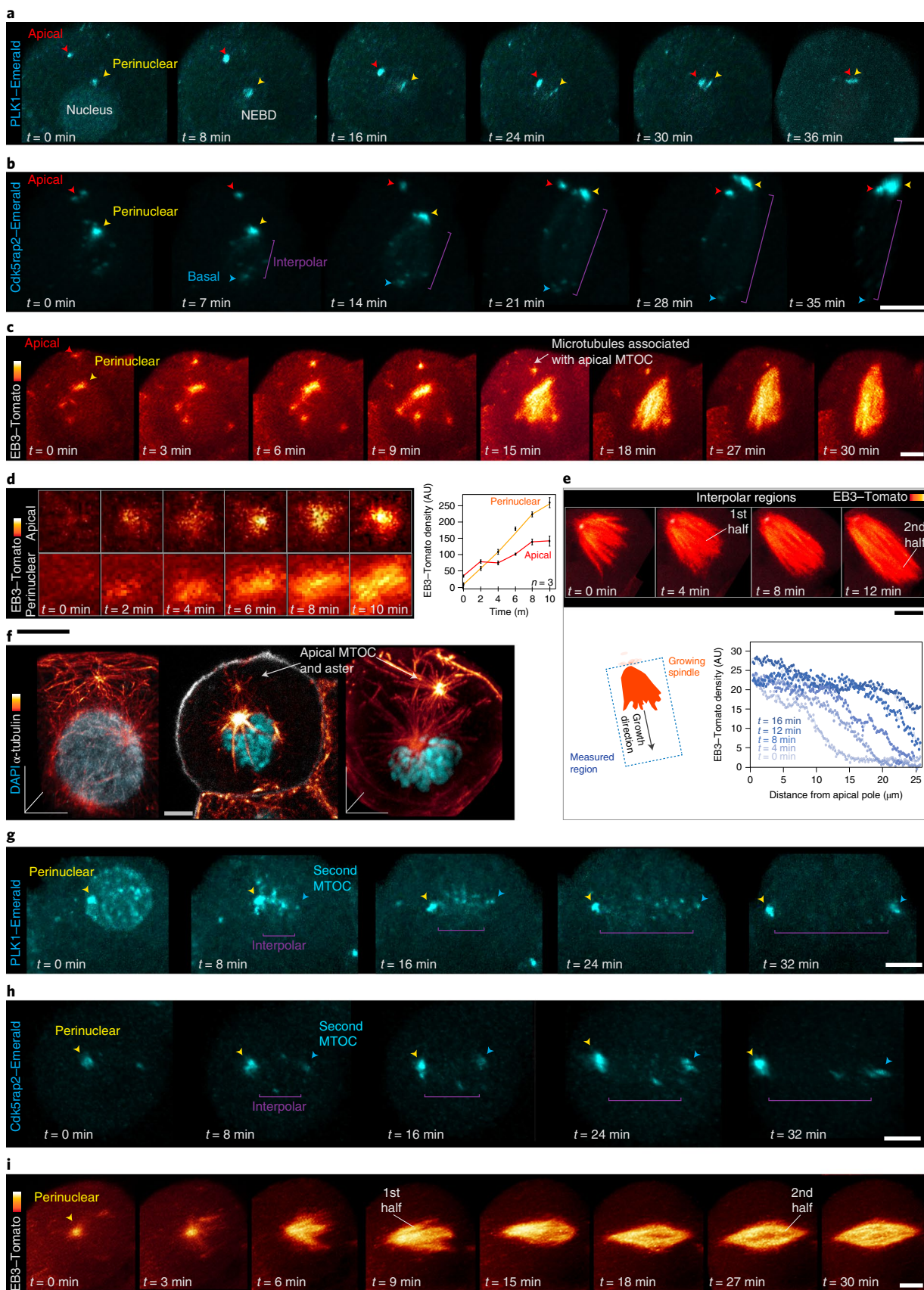


**Fig. 1 | A monoastral mitotic spindle in the mouse embryo. a**, Mouse embryos immunolabelled at the 4-cell stage, 16-cell stage and blastocyst stage with  $\alpha$ -tubulin antibodies. Mitotic spindles display relatively similar spindle halves and few or no detectable astral microtubule arrays. Data are from three independent experiments. **b**, An 8-cell embryo, showing a cell with a monoastral mitotic spindle displaying a single astral-like array on the apical side. **c**, Magnified views of monoastral and anastral spindles in 8-cell embryos. Note the presence of a large aster on the apical side of the monoastral spindle. Data in **b,c**, are from seven independent experiments. **d**, Comparison of microtubule density probed by  $\alpha$ -tubulin between the apical and basal sides of the monoastral spindle, or between the two sides (A and B) of anastral spindles. The centre line of the box is the median, box edges delineate upper and lower quartiles and whiskers represent the range. \*\*\*\* $P < 0.0001$ ; two-tailed Mann-Whitney  $U$ -test (4- to 8-cell, 8-cell anastral, 16- to 32-cell, and blastocyst) and unpaired Student's  $t$ -test (8-cell monoastral). AU, arbitrary units. **e**, Frequencies of monoastral spindles and inner cells at the 16-cell stage are similar ( $P = 0.98$ , Kolmogorov-Smirnov test). NS, not significant. Scale bars, 5  $\mu$ m in xyz space.



Extended Data Fig. 2j). The downstream PLK1 target Cdk5rap2 (tracked using Cdk5rap2-Emerald) involved in microtubule nucleation<sup>30</sup> reveals a similar localization pattern (Fig. 2b,h and Extended

Data Fig. 2m). Tracking EB3-Tomato comets demonstrates that both structures function as non-centrosomal MTOCs (Fig. 2c,d and Extended Data Fig. 2g,k).

**Fig. 2 | The monoastral spindle is assembled by two separate MTOCs in different subcellular regions.** **a,b**, Live imaging of PLK1–Emerald (**a**) and Cdk5rap2–Emerald (**b**) in single cells of the 8-cell embryo show two structures at the apical cell cortex and perinuclear regions. Tracking with high resolution shows how they approach over time following NEBD. Data are from five independent experiments. **c**, Live imaging of EB3–Tomato identifies apical and perinuclear structures similar to those detected in **a,b**. **d**, These EB3–Tomato-positive puncta show an increase in microtubule growth emanating from them over time, indicating that they start to function as MTOCs. Graph shows EB3–Tomato fluorescence intensity over time. Data are mean  $\pm$  s.e.m.; data in **c,d**, are from seven independent experiments. **e**, Live imaging of EB3–Tomato and schematic show that the interpolar parts of the spindle assemble in a directional manner, starting with one spindle half and then continuing with the other. Graph shows fluorescence over time along the spindle. Data are from eight independent experiments. **f**,  $\alpha$ -Tubulin immunofluorescence and DAPI in non-injected 8-cell embryos. Left: a cell in interphase. Centre and right: cells in mitosis. Note the appearance of bona fide apical and perinuclear MTOCs displaying high microtubule density. Data are from three independent experiments. **g–i**, Live imaging of PLK1–Emerald (**g**), Cdk5rap2–Emerald (**h**) and EB3–Tomato (**i**) in single cells of the 8-cell embryo show their dynamics during anastral spindle formation. Unlike the monoastral spindle (**a–c**), these cells only establish the perinuclear MTOC. The intensities of PLK1–Emerald, Cdk5rap2–Emerald and EB3–Tomato are initially higher at the spindle pole that forms first, but become balanced as the second spindle half emerges. Data are from five (**g,h**) to seven (**i**) independent experiments. Scale bars, 10  $\mu$ m.

The apical MTOC initiates the astral array (Fig. 2f and Extended Data Fig. 2f,h). By contrast, the perinuclear MTOC establishes the interpolar regions. These interpolar regions assemble in an unusual directional manner, starting proximal to the perinuclear MTOC and then proceeding towards the basal region (Fig. 2c,e and Extended Data Fig. 2g). Moreover, while the astral and interpolar regions appear in different locations, they gradually move towards each other (Fig. 2a–c and Extended Data Fig. 2g,m). By contrast, cells with anastral spindles do not establish a stable apical MTOC (Fig. 2g–i). In 15% of cells, a transient apical MTOC is initially detected but disappears before metaphase (Extended Data Fig. 2l,o).

**The monoastral spindle is highly asymmetric.** We further investigated the organization of the monoastral spindle and found that its metaphase plate is positioned closer to the basal cortex than in anastral spindles (Fig. 3a,c). The basal positioning of the metaphase plate of the monoastral spindle is accounted by the presence of the astral array. Eight-cell-stage blastomeres have an average diameter of  $31.4 \pm 2.4 \mu$ m on the apical–basal axis. The astral array introduces a  $3.1 \pm 0.9 \mu$ m gap, separating the apical spindle pole and cortex (Fig. 3a,c). Moreover, the apical region is  $1 \pm 0.4 \mu$ m longer than the basal (Fig. 3c), has a higher microtubule density (Extended Data Fig. 3b) and displays more EB3–Tomato comets (Fig. 3c–e and Supplementary Video 2). These asymmetries are consistent with higher levels of PLK1–Emerald and Cdk5rap2–Emerald in the apical pole (Fig. 2a,b and Extended Data Fig. 2m,n). The apical region also displays more  $\alpha$ -tubulin tyrosination, a proxy for enhanced microtubule dynamics<sup>31</sup> (Fig. 3d). Conversely, the levels of HURP, which is associated with less dynamic microtubules<sup>32</sup>, are higher on the basal half (Fig. 3d). These parameters are more symmetric in anastral spindles (Fig. 3c–e, Extended Data Fig. 3b and Supplementary Video 2). Thus, the monoastral spindle is highly

asymmetric in composition, has its metaphase plate off-centre and displays increased growth on its apical region.

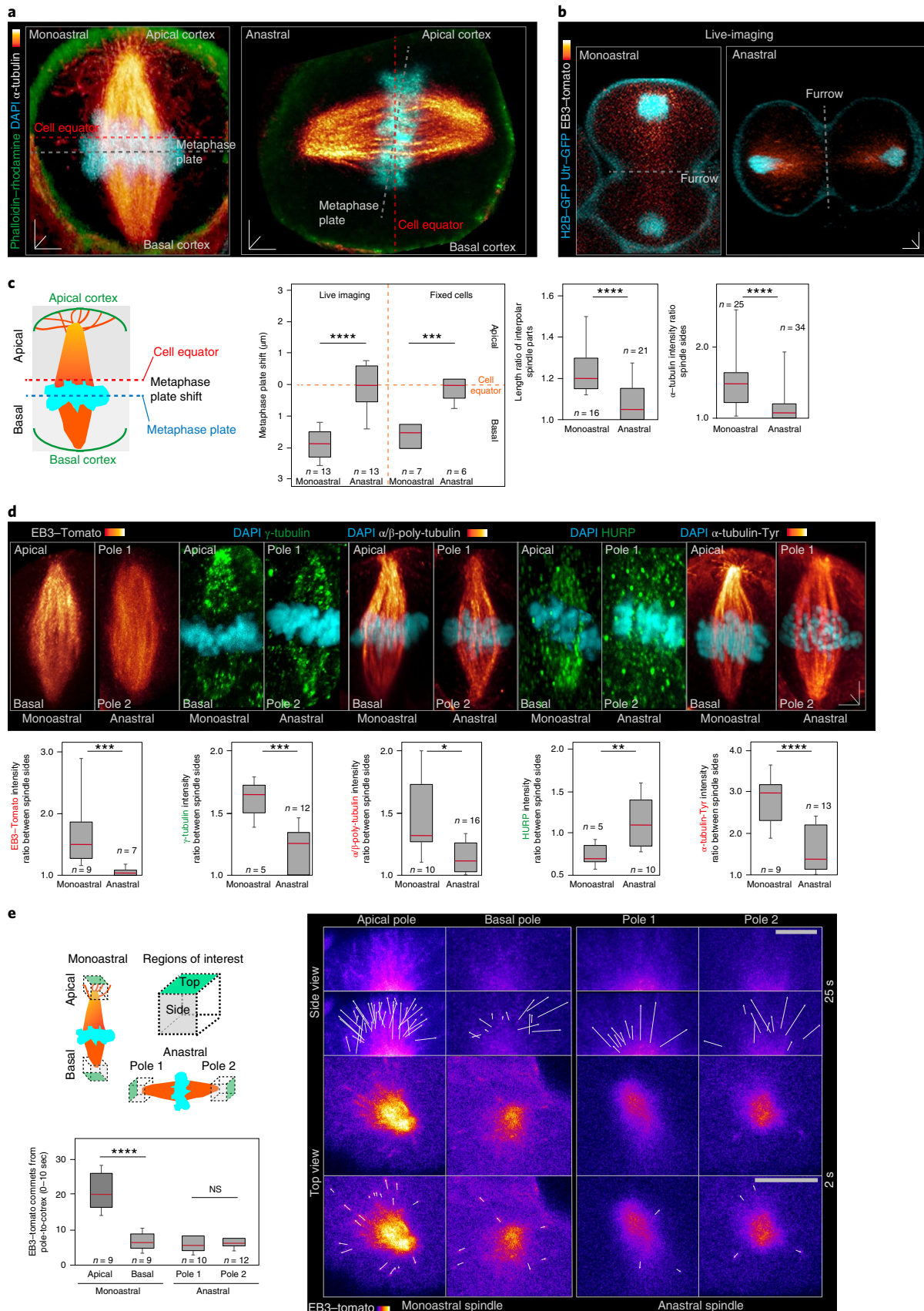
**The monoastral spindle causes asymmetric division patterns.** Sixteen-cell stage embryos contain two to three inner cells<sup>3,13,33</sup>—similar to the number of blastomeres assembling monoastral spindles (Fig. 1e). Consistently, tracking of division patterns shows that most inner cells derive from cells with monoastral spindles, whereas anastral spindles produce outer–outer daughters (Fig. 4a,b). Furthermore, cells with monoastral spindles divide more orthogonally to the apical surface (Fig. 4c). In more orthogonal divisions, the basal daughter is positioned closer to the embryo's centre of mass and has a larger area crowded by E-cadherin interactions<sup>3</sup> (Extended Data Fig. 4a). Moreover, following internalization, inner cells do not delocalize to the outer region<sup>3</sup>, which probably results from increased E-cadherin contacts. In line with this, loosening E-cadherin interactions using DECMA1 antibodies shifts cells from inner to outer positions (Extended Data Fig. 4b). Thus, by triggering more orthogonal divisions, the monoastral spindle favours inner cell allocation.

In addition, the asymmetric positioning of the metaphase plate and cleavage furrow of the monoastral spindle produces daughters of different volumes, with inner cells smaller than outer cells<sup>34</sup> (Figs. 3b and 4d and Extended Data Figs. 3a and 5h). Decreasing cell size amplifies cortical tension and enables internalization<sup>35</sup> and could facilitate apical constriction in the embryo<sup>3</sup>. To explore this, we imaged green fluorescent protein (GFP)–myosin II in live embryos. In line with two types of spindle organization, the videos reveal two modes of division: in 69% of cases ( $n=9$  cells), GFP–myosin II accumulates symmetrically in dividing cells and the cleavage furrow forms near the equator, producing daughters of similar size. By contrast, in 31% of cases ( $n=4$  cells) in which

**Fig. 3 | Asymmetric organization of the monoastral mitotic spindle.** **a**,  $\alpha$ -Tubulin immunofluorescence, and phalloidin–rhodamine and DAPI staining in non-injected 8-cell embryos comparing a monoastral and anastral mitotic spindle. The monoastral spindle is oriented more orthogonal to the apical cortex and its metaphase plate is positioned asymmetrically, closer to the basal cortex. By contrast, the anastral spindle is oriented less orthogonal and the metaphase plate is positioned more symmetrically within the cell. **b**, Live imaging of cell divisions of parental cells with a monoastral or anastral spindles reveal different division patterns. The cell with a monoastral mitotic spindle divides more orthogonal and generates a larger outer cell and smaller inner cell. **c**, Scheme shows the main parts of the monoastral mitotic spindle analysed. Graphs show differences between monoastral and anastral spindles in metaphase plate positioning, length of the apical versus basal parts and overall microtubule density probed by  $\alpha$ -tubulin. \*\*\* $P=0.0006$  (immunofluorescence, Mann–Whitney  $U$ -test), \*\*\*\* $P<0.0001$  (live imaging, two-tailed unpaired Student's  $t$ -test) for metaphase plate shift analyses. \*\*\*\* $P=0.0008$  (length ratio, two-tailed Mann–Whitney  $U$ -test), \*\*\*\* $P<0.0001$  (intensity ratio, unpaired Student's  $t$ -test). **d**, Characterization of additional asymmetric features between monoastral and anastral spindle organization. Note the increased microtubule density at the apical parts of the monoastral spindle, probed with EB3–Tomato,  $\alpha$ -tubulin, polyglutamylated and tyrosinated. HURP levels, by contrast, are higher in the basal parts. All these markers display a more symmetric distribution in anastral spindles. Anastral spindles have a more parallel orientation but are aligned next to monoastral ones to facilitate comparison. \*\*\* $P=0.0005$  (EB3–Tomato); \* $P=0.0187$  ( $\alpha/\beta$ -poly-tubulin), \*\* $P=0.008$  (HURP); unpaired two-tailed Student's  $t$ -test. \*\*\* $P=0.0008$  ( $\gamma$ -tubulin), \*\*\*\* $P<0.0001$  ( $\alpha$ -tubulin–Tyr); unpaired two-tailed Mann–Whitney  $U$ -test. **e**, Scheme shows areas of quantification of EB3–Tomato comets. The apical parts of the monoastral spindle display increased microtubule growth than the basal regions. In anastral spindles, the two poles display similar dynamics. \*\*\*\* $P<0.0001$ ; Unpaired two-tailed Mann–Whitney  $U$ -test. In box plots, the centre line is the median, box edges delineate upper and lower quartiles and whiskers represent the range. Scale bars, 5  $\mu$ m.

GFP–myosin II accumulates closer to the basal cortex, the inner cell is 28% smaller (Extended Data Fig. 4c). This difference in volume occurs in highly orthogonal divisions as well as in divisions

followed by apical constriction (Fig. 4d). Notably, comparing these patterns to the spindle of the parental cell confirms that monoastral cells produce daughters with unequal volumes, whereas anastral cells



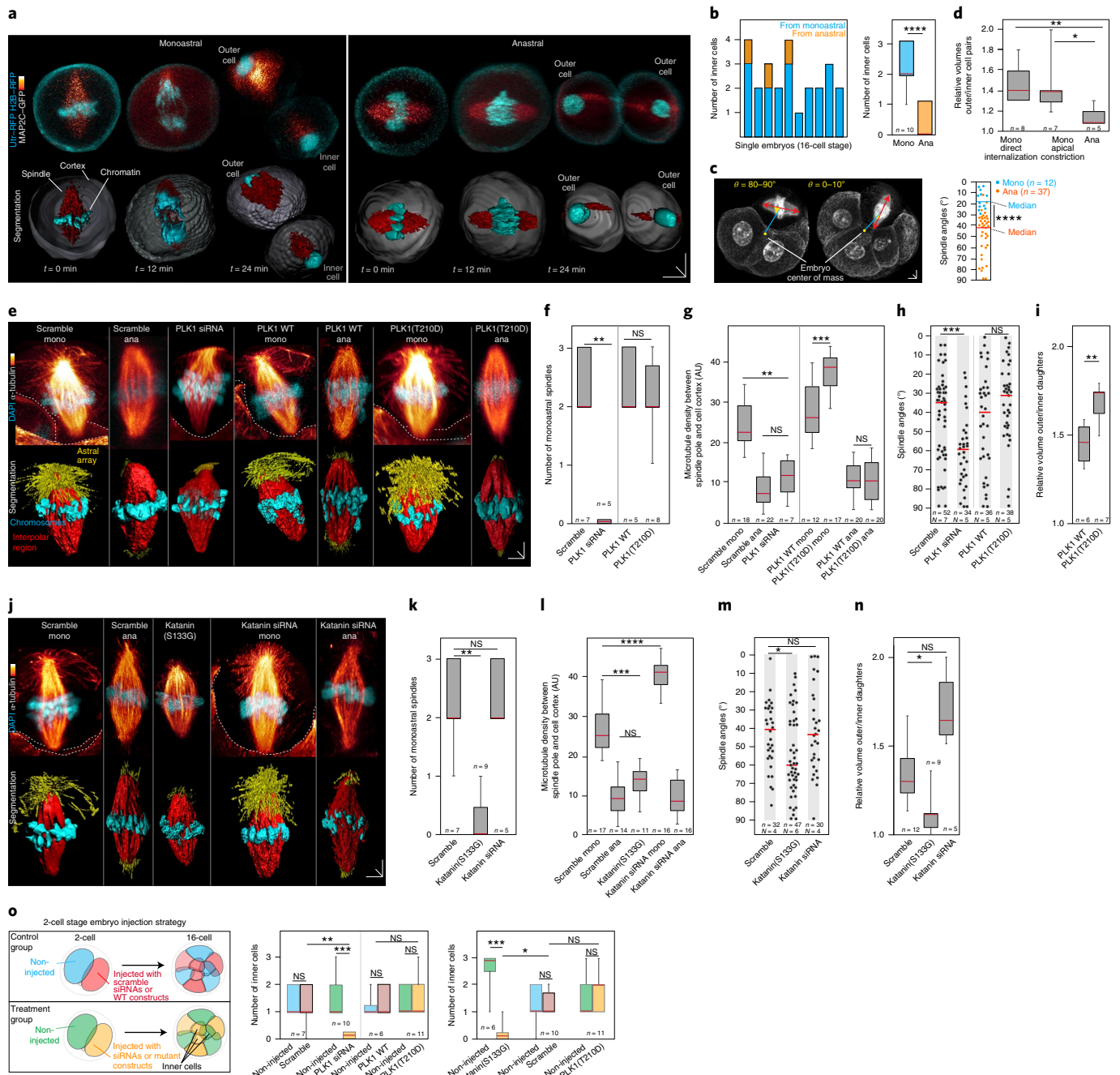


**Fig. 4 | The monoastral spindle drives asymmetric cell division.** **a**, Live imaging and computer segmentation of cells displaying monoastral and anastral spindles during division. **b**, Preferential generation of inner cell progeny by cells with monoastral spindles. Left graph shows number of 16-cell embryos analysed.  $****P < 0.0001$ ; two-tailed Mann-Whitney  $U$ -test. Ana, anastral; mono, monoastral. **c**, Scheme shows quantification of spindle orientation. The graph shows more orthogonal angles in cells with monoastral spindles (blue).  $****P < 0.0001$ ; Mann-Whitney  $U$ -test. **d**, Ratio of outer/inner cell volumes.  $*P = 0.0266$ ,  $**P = 0.008$ ; Kruskal-Wallis test. **e**, Staining followed by computer segmentation in 8-cell embryos shows how manipulations of PLK1 affect the size of the astral array. WT, wild type. **f-i**, Number of monoastral spindles (**f**), differences in microtubule density at the apical pole where the astral array normally forms (**g**), spindle angle (**h**) and relative daughter cell volumes (**i**) after PLK1 manipulations. In (**h**),  $n$  and  $N$  are number of spindles and embryos, respectively.  $**P = 0.0005$ , two-tailed unpaired Student's  $t$ -test (**h**);  $**P = 0.0013$ , two-tailed Whitney  $U$ -test (**f**);  $***P = 0.0003$ , two-tailed Whitney  $U$ -test (**g**);  $**P = 0.0047$ , two-tailed Whitney  $U$ -test (**i**).  $**P = 0.0036$ , Kruskal-Wallis test (**g**). **j**, Examples of katanin manipulations. **k-n**, Effect on the number of monoastral spindles (**k**), differences in microtubule density at the apical pole (that is, astral array) (**l**), spindle angle (**m**) and relative daughter cell volumes (**n**). In (**m**),  $n$  and  $N$  are number of spindles and embryos, respectively.  $*P = 0.0206$  (**m**);  $*P = 0.0152$  (**n**);  $**P = 0.0023$  (**k**);  $***P = 0.0006$  (**l**); two-tailed Kruskal-Wallis test (**k-l**);  $****P < 0.0001$ ; two-tailed Mann-Whitney  $U$ -test (**l**). **o**, Left: scheme showing 2-cell stage injection strategy. Centre, right: number of inner cells derived from non-injected cells versus cells injected with controls or treatments within the same 16-cell stage embryo.  $*P = 0.0272$ ,  $**P = 0.0027$ ,  $***P = 0.0001$  (PLK1);  $***P = 0.0002$  (katanin); Kruskal-Wallis test. In box plots, the centre line is the median, box edges delineate upper and lower quartiles and whiskers represent the range. Scale bars, 10  $\mu\text{m}$  (**a**); 5  $\mu\text{m}$  (**c**); 3  $\mu\text{m}$  (**e, j**).

produce similarly sized daughters (Fig. 4d and Extended Data Fig. 5f). Therefore, division patterns and inner–outer segregation are not stochastic processes<sup>10–12</sup>, but are predicted by spindle type.

Deletion of the *Plk1* gene results in developmental arrest prior to lineage segregation<sup>36</sup>. Thus, we established a knockdown approach that decreases the level of PLK1 protein (Extended Data Fig. 5b). We microinjected one cell of 2-cell embryos with small interfering RNAs (siRNAs), which enables direct comparison of knockdown and control cells. Cells in which PLK1 is reduced do not establish monoastral spindles (Fig. 4e–g). Instead, they form only inter-polar regions and display division patterns similar to control cells with anastral spindles: they have more parallel division angles, produce daughters with similar volumes and do not contribute inner progeny (Fig. 4h,o and Extended Data Fig. 5i). Similarly, treatment with the PLK1 inhibitor volasertib reduces monoastral spindle and inner cell numbers and produces daughters of similar volume (Extended Data Fig. 5d,e,i). By contrast, microinjection of mRNA for the constitutively active phospho-mimicking mutant PLK1(T210D)–Emerald<sup>37</sup> increases aster size (Fig. 4e,g). PLK1(T210D)–Emerald-overexpressing cells also display more pronounced asymmetries in daughter volume (Fig. 4i). Yet, the proportion of PLK1(T210D)–Emerald-overexpressing cells assembling monoastral spindles and their inner cell contribution remain similar to that of control cells (Fig. 4f,o). This suggests that some factor that is differentially regulated between cells of the embryo restricts the number of cells assembling monoastral spindles.

We then used the p60 catalytic subunit of the microtubule-severing protein katanin<sup>38</sup>. Microinjection of a katanin S133G mutant with increased activity (Extended Data Fig. 5a) prevents aster formation (Fig. 4j–l). These cells establish shorter and symmetric spindles, and their daughter cells rarely internalize (Fig. 4o and Extended Data Fig. 5m–o). The retention of katanin(S133G)-overexpressing cells in the outer region is consistent with parallel division patterns and symmetric daughter volumes (Fig. 4m,n). Finally, microinjection of siRNAs targeting the katanin p60 subunit increases the size of the apical aster, yet the proportion of cells assembling monoastral spindles and their contribution to inner progeny are similar to those of non-injected cells (Fig. 4j–l,o).

**Monoastral spindle components are inherited asymmetrically.** After division, outer cells establish a cortical F-actin ring that enriches apical polarity proteins<sup>25,26</sup> to differentially regulate Yap–Cdx2. F-actin rings also prevent apical constriction to retain trophectoderm-specified cells in an outer position<sup>26</sup>. We showed that a network of microtubules appears under the apical cortex after division to clear F-actin and trigger ring formation. By contrast, internalizing cells never establish F-actin rings<sup>26,39</sup>. Yet a key question remains over which mechanism regulates differential ring

formation<sup>9</sup>. Imaging of divisions shows that the apical regions of the monoastral spindle are rapidly pulled against the cortex after mitosis, triggering a burst of F-actin and myosin II where the nucleus bounces against the cortex (Fig. 5a–c, Extended Data Fig. 6a and Supplementary Videos 3 and 4). This ‘cortex-bouncing’ event delivers microtubules to the cortex, where F-actin is cleared to form the ring (Fig. 5d and Extended Data Fig. 6a,b). By contrast, the basal regions do not display this behaviour and consistently, the basal daughter inherits fewer microtubules, does not clear F-actin, does not form a ring and internalizes (Figs. 5a–d and 6a–c, Extended Data Fig. 6a–d and Supplementary Video 3).

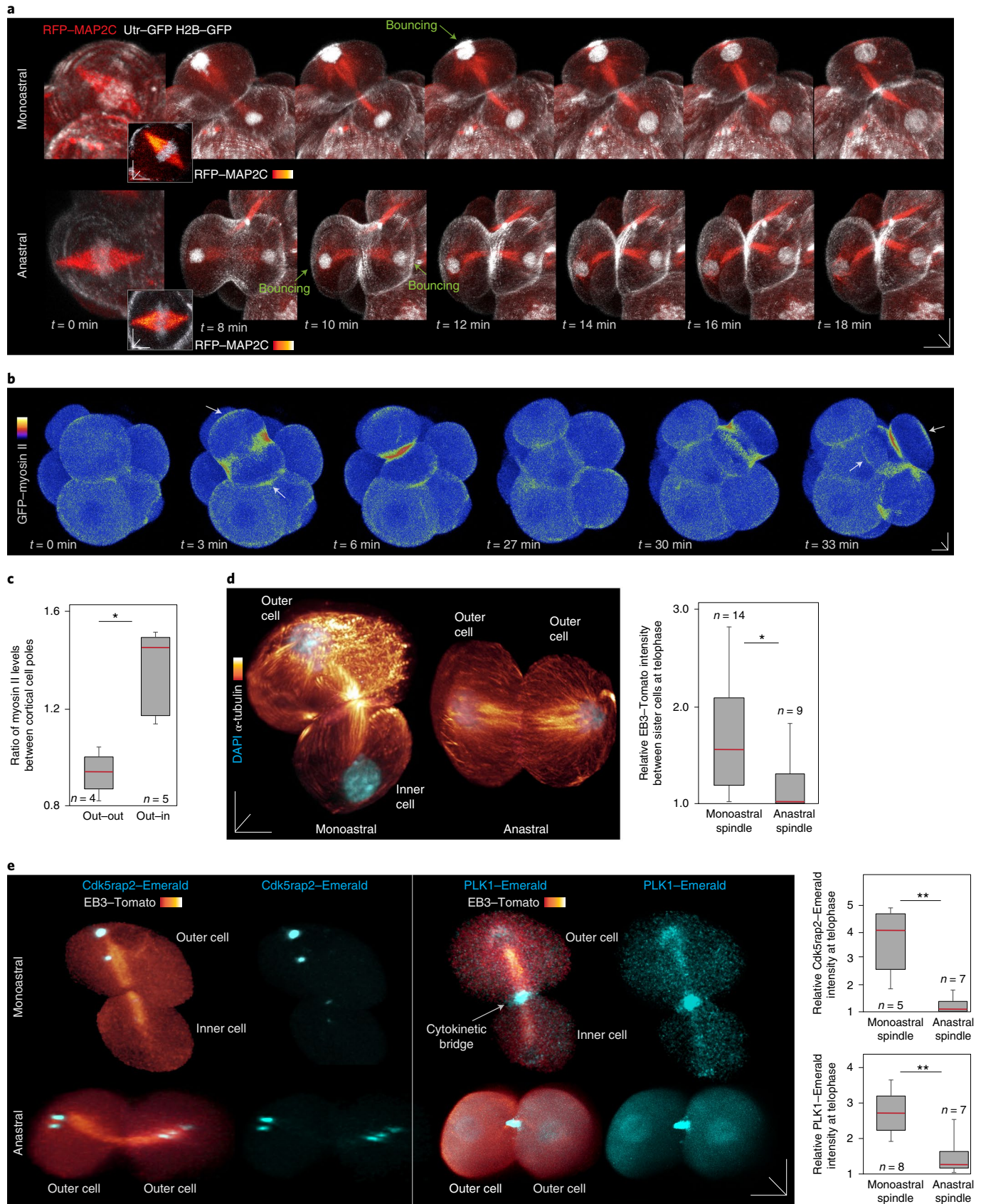
The microtubule network inherited under the cortex is present for at least 2 h after division (Extended Data Fig. 6c,e). Consistent with this, imaging divisions uncovers an asymmetric inheritance of Cdk5rap2–Emerald in cells with monoastral spindles (Fig. 5e), indicating that in addition to delivering unequal networks of microtubules, the monoastral spindle drives asymmetric inheritance of microtubule regulators. While most of PLK1–Emerald remains at the midbody, a fraction is also asymmetrically inherited with the apical parts of the spindle (Fig. 5e). For cells with anastral spindles, the two outer daughters display a bouncing behaviour, albeit less pronounced than that of outer cells derived from a monoastral spindle (Fig. 5a,c and Supplementary Videos 3 and 4). Consistently, the two outer daughters symmetrically inherit a smaller microtubule network and lower Cdk5rap2–Emerald and PLK1–Emerald levels than outer cells derived from monoastral spindles (Fig. 5d,e and Extended Data Fig. 6b). Furthermore, they form smaller rings (Fig. 6c and Extended Data Fig. 6d). Consistent with the role of F-actin rings in polarization, the outer cell inheriting the apical parts of the monoastral spindle enriches Ezrin–GFP apically, whereas cells inheriting the basal region lack Ezrin–GFP (Fig. 6b). Thus, two types of spindle organization determine differential ring formation and polarization.

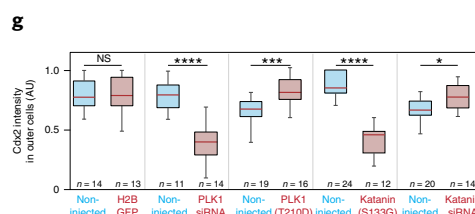
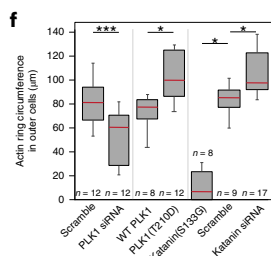
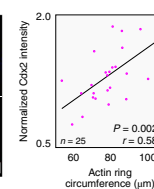
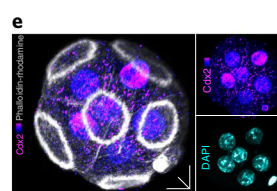
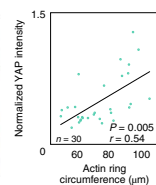
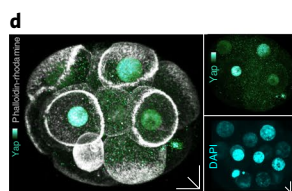
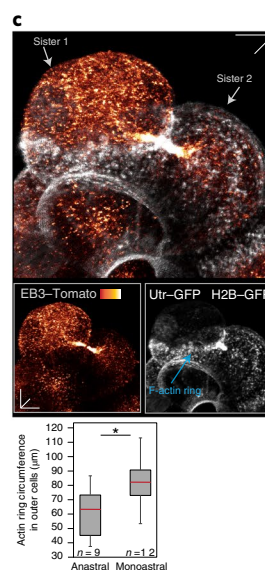
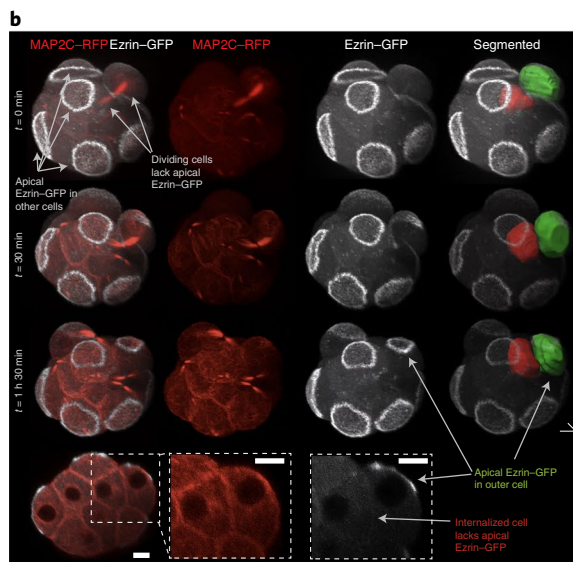
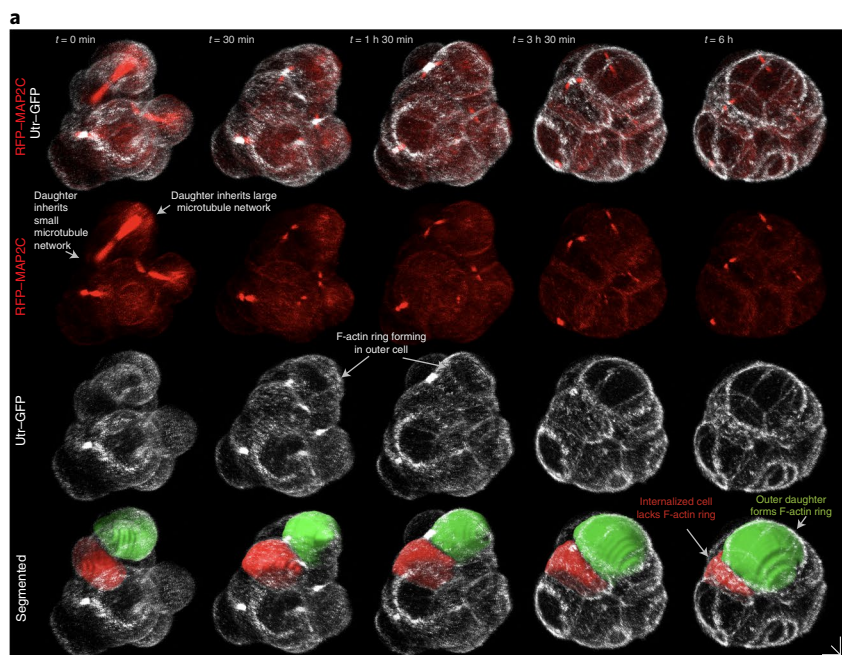
Finally, we tested how spindle manipulations affect ring formation and fate. First, we confirmed the model proposing that polarization is important for lineage fate and found that cells with rings and Ezrin–GFP display higher nuclear Yap and Cdx2 levels (Fig. 6d,e and Extended Data Fig. 7a). Consistently, disrupting F-actin using latrunculin A or the dominant-negative RhoA mutant RhoA(T19N), reduces Cdx2 (Extended Data Fig. 7a). In line with their effects on spindle organization, PLK1(T210D)–Emerald and katanin siRNAs trigger inheritance of larger microtubule networks under the cortex of outer cells, formation of larger rings and high Cdx2 levels (Fig. 6f,g and Extended Data Figs. 6e and 7b). By contrast, PLK1 siRNAs or katanin(S133G) cause the opposite effects (Fig. 6f,g and Extended Data Figs. 6e and 7b). Thus, the monoastral spindle regulates inner–outer cell segregation and fate.

**Fig. 5 | Asymmetric inheritance of microtubules and microtubule regulators from the monoastral spindle during cell division.** **a**, Live imaging reveals additional asymmetries during the division resulting from monoastral versus anastral spindles. In cells with monoastral spindles, the apical parts of the spindle and the newly forming outer nucleus bounce against the cortical pole. This cortex-bouncing behaviour is evidenced by a transient accumulation of cortical F-actin (Utr-GFP) at the site of bouncing (arrow). By contrast, the future inner cell inherits the basal parts of the monoastral spindle. This part has a smaller microtubule network, and the newly forming cell nucleus does not bounce against the cortex. Instead, the nucleus is directly positioned closer to the centre of mass of the cell. Bottom row: the division sequence of a cell with an anastral mitotic spindle. The two outer daughters inherit a similar amount of microtubules and display more moderate cortex bouncing compared with the outer cell from the monoastral spindle (top row). Insets show asymmetric microtubule intensity in the apical region of the monoastral spindle at the start of imaging experiment. **b**, Consistent with the cortex-bouncing behaviour in **a**, live imaging of GFP–myosin II with high spatiotemporal resolution and quantification of fluorescence levels between the resulting cell poles reveals strong cortex-bouncing behaviour in an outer cell. **c**, GFP–myosin II levels at the apical cortex in **b** (\**P* = 0.0159; two-tailed Mann–Whitney *U*-test). **d**, Staining in non-injected 8-cell embryos confirms the inheritance of a larger microtubule network by the outer cell in a division producing an outer–inner daughter pair. By contrast, outer–outer daughters derived from parental cells with anastral spindles inherit similar amounts of microtubules. The graph confirms the more asymmetric inheritance of microtubules by outer cells resulting from outer–inner than outer–outer divisions (\**P* = 0.0232; two-tailed Mann–Whitney *U*-test). **e**, Live imaging shows asymmetric inheritance of Cdk5rap2–Emerald and PLK1–Emerald in divisions originating from monoastral spindles (\*\**P* = 0.0025 (Cdk5rap2); \*\**P* = 0.0023 (PLK1); two-tailed Mann–Whitney *U*-test). In box plots, the centre line is the median, box edges delineate upper and lower quartiles and whiskers represent the range. Scale bars, 10 μm.

**Keratins differentially regulate spindle formation.** A final question is why only a subset of cells establishes monoastral spindles. In *C. elegans*, apical domains stabilize non-centrosomal MTOCs<sup>40</sup>.

Furthermore, a small proportion of cells with anastral spindles initially displays an apical MTOC, but this disappears prior to the assembly of a complete spindle apparatus (Extended Data Fig. 2l).





Thus, we disrupted the cortex using cytochalasin D. This caused multiple ectopic MTOC-like structures (Extended Data Fig. 8a), consistent with a role of the cortex in regulating MTOCs. We then

tested downregulation of the apical domain protein Pard6b<sup>26,41</sup>, which prevented the appearance of apical MTOCs. Instead, knock-down cells form an MTOC near the lateral junctions, which

**Fig. 6 | Spindle manipulations disrupt division patterns and inner-outer cell segregation.** **a, b**, Live imaging of RFP-MAP2C and Utr-GFP (**a**) or RFP-MAP2C and Ezrin-GFP (**b**) show the establishment F-actin rings and apical polarization in outer cells derived from monoastral spindles. The daughter cell inheriting the basal parts of the spindle does not form a ring, does not enrich apical Ezrin-GFP, and internalizes. Data are from four (**a**) or five (**b**) independent experiments. **c**, Live imaging of EB3-Tomato, Utr-GFP and H2B-GFP shows that 16-cell stage blastomeres positioned in the outer parts of the embryo and displaying a larger microtubule network under the cell cortex form large F-actin rings. By contrast, the outer daughter with a smaller microtubule network displays a smaller ring. Bottom: outer cells with siblings that have internalized have larger rings than daughter cells with outer siblings ( $*P=0.0148$ ; two-tailed Mann-Whitney *U*-test). Data are from five independent experiments. **d, e**, Immunofluorescence and quantification of actin ring circumference in 3D (see Methods) shows that cells with larger F-actin rings have higher levels of nuclear Yap and Cdx2 (Spearman's correlation). Data are from three (**d**) or five (**e**) independent experiments. **f**, Manipulations of PLK1 and katanin affect F-actin ring circumference.  $*P=0.0487$  (katanin);  $*P=0.0455$  (katanin siRNA); Kruskal-Wallis test.  $*P=0.0201$  (PLK1(T210D));  $***P=0.0009$  (PLK1 siRNA); two-tailed Mann-Whitney *U*-test. **g**, Effect of manipulations of PLK and katanin on Cdx2 levels in outer cells ( $*P=0.0187$ ,  $***P=0.0003$ ,  $****P<0.0001$ ; two-tailed Mann-Whitney *U*-test). In box plots, the centre line is the median, box edges delineate upper and lower quartiles and whiskers represent the range. Scale bars, 10  $\mu$ m.

subsequently joins the spindle (Extended Data Fig. 8e). Moreover, they generate fewer monoastral spindles, divide more parallel and contribute fewer inner cells (Fig. 7d,e,g). Conversely, a high dose of SiR-actin, which stabilizes the cortex<sup>25</sup>, increases inner cell numbers (Extended Data Fig. 8d). Thus, the apical cortex facilitates apical MTOC formation, yet it is unclear why this occurs only in a subset of cells.

A previous study suggested that the size of the apical domain regulates spindle orientation<sup>24</sup>. However, imaging apical domains in live embryos shows no correlation between domain size and spindle orientation (Extended Data Fig. 8b). Furthermore, the apical domain disassembles before the metaphase spindle is fully assembled<sup>26</sup>. Thus, differences in timing of apical domain disassembly, rather than size, may differentially regulate spindle formation. Imaging of divisions shows that the apical domain disassembles by interphase-prophase in most cells (Fig. 7a and Extended Data Fig. 8c), but in cells with monoastral spindles it is retained for longer ( $45 \pm 19$  min and  $24 \pm 24$  min, respectively) until prophase-metaphase (Fig. 7a). This confirms that some factor differentially regulates the stability of the cortex and spindle assembly. Thus, we investigated a role for keratins, which are differentially regulated within the embryo and stabilize cortical F-actin<sup>25</sup>.

Importantly, 8-cell blastomeres assembling keratin filaments correspond to those establishing monoastral spindles (Fig. 7b-d). Moreover, live imaging of keratin 8 fused to Emerald (Krt8-Emerald) shows that the apical domain is maintained for longer in cells with keratins (Fig. 7c,f). We then microinjected siRNAs targeting Krt8 and Krt18, which reduced the establishment of monoastral spindles (Fig. 7d). Furthermore, although the spindle initially adopts an orthogonal orientation in some cells in which Krt8 and Krt18 are knocked down, this alignment is gradually lost (Fig. 7h). Consistently, knockdown of Krt8 and Krt18 causes cells to divide with more parallel orientations and produce predominantly outer progeny (Fig. 7e,g). Finally, microinjecting a high concentration of

Krt8 and Krt18 mRNAs<sup>25</sup> increases the proportion of cells assembling monoastral spindles and the contribution of inner cell progeny (Fig. 7d,g). Thus, heterogeneities in keratin filament assembly differentially regulate the timing of apical domain disassembly to determine monoastral spindle assembly.

## Discussion

Here we show that inner-outer cell segregation and trophectoderm-pluripotent specification are not stochastic<sup>10,11</sup>, but are determined by two types of spindle organization. Similar to meiotic spindles forming without centrosomes<sup>42,43</sup>, most blastomeres assemble anastral spindles, which trigger symmetric division patterns producing outer-outer daughters. By contrast, the monoastral spindle drives more orthogonal cleavage planes and differences in cell volume. In addition, asymmetric inheritance of microtubules and microtubule regulators from its apical parts trigger differential regulation of F-actin rings, which provides a mechanism to differentially regulate polarization and Cdx2 expression (Extended Data Fig. 9).

The most prominent feature of the monoastral spindle is its astral array. Single asters were found in cells treated with kinesin inhibitors<sup>44</sup>. By contrast, the monoastral spindle has two poles but assembles only one aster. Others have observed spindles with asymmetric asters, but those arose from differential regulation of centrosomes<sup>45-47</sup>. The aster of the monoastral spindle originates from a non-centrosomal MTOC. Furthermore, this apical MTOC initiates aster assembly distant from the nucleus, and later joins the rest of the spindle assembled by the perinuclear MTOC. We cannot determine whether these MTOCs fuse to form a single MTOC or remain as independent MTOCs. Nevertheless, unlike classical models of mitotic spindle formation, where asters originate from centrosomes<sup>48</sup>, the main components of the monoastral spindle assemble in a modular manner, starting in separate regions.

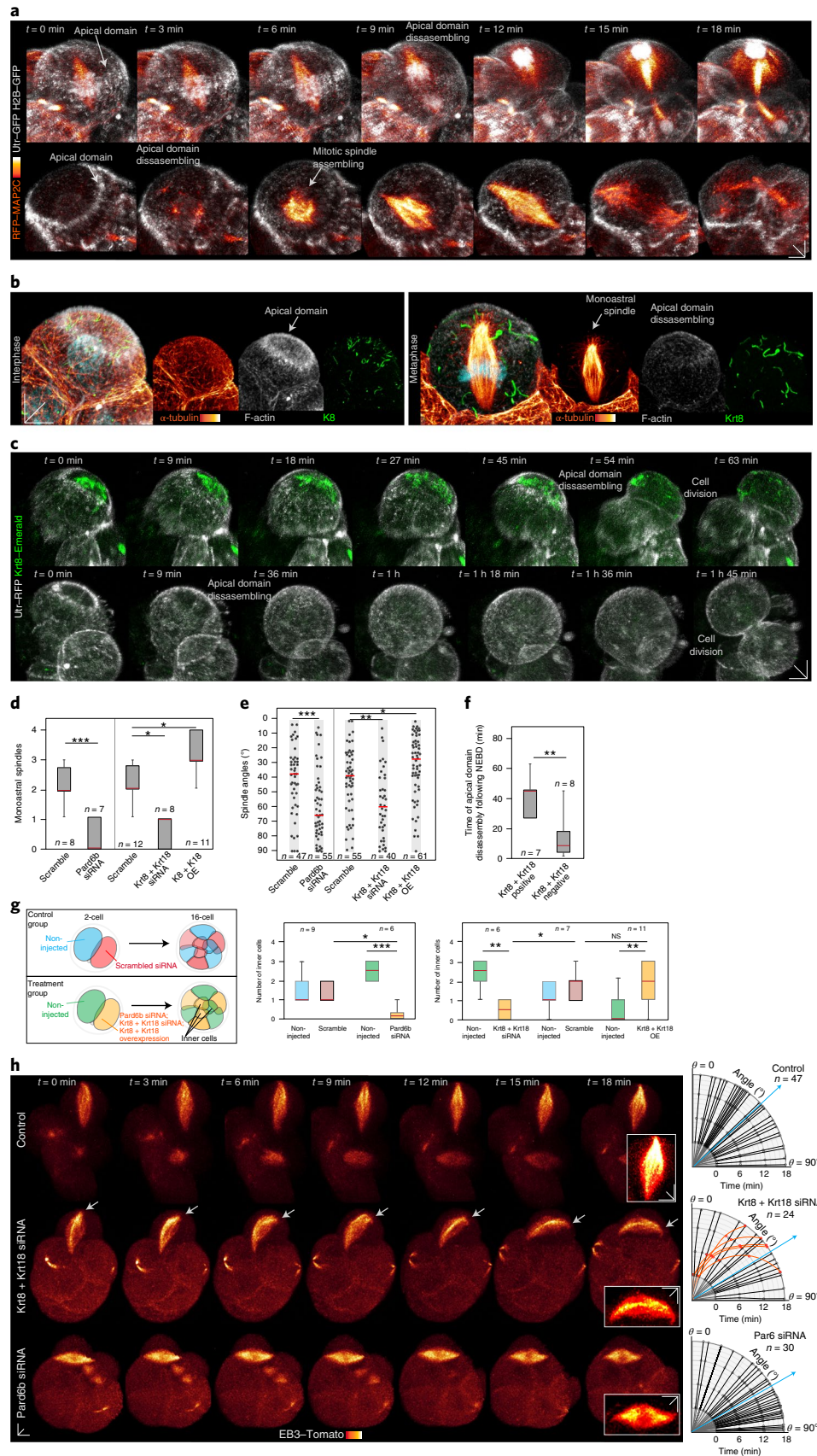
PLK1-positive puncta are initially detected at the apical cortex of some blastomeres, yet only a subset of cells converts them into

## Fig. 7 | Heterogeneities in keratin filament assembly differentially stabilize the cell cortex to trigger monoastral spindle formation in a subset of cells.

**a**, Live imaging of cell divisions. During division of cells with a monoastral spindle, the apical domain disassembles later than in anastral spindles, after the spindle starts to form. **b**, Immunofluorescence in non-injected 8-cell embryos. In cells expressing keratins, the apical domain is clearly present during interphase and it disassembles during metaphase. **c**, Live imaging shows that the apical domain is more stably retained at the apical cortex during mitosis and disassembles just before division in a cell expressing keratins. By contrast, in a cell without keratins from the same embryo, the apical domain disassembles prior to division. **d**, Proportion of 8-cell stage blastomeres forming a monoastral spindle following microinjections at the 1-cell stage.  $*P=0.0145$  (Krt8 + Krt18 siRNA),  $*P=0.0309$  (Krt8 + Krt18 overexpression); Kruskal-Wallis test.  $***P=0.0006$ ; two-tailed Mann-Whitney *U*-test. OE, overexpression. **e**, Pard6b and keratin manipulations affect division angles. Embryos were injected at the 1-cell stage as in **d**.  $*P=0.0416$ ,  $**P=0.0015$ ,  $***P=0.0009$ ; two-tailed Student's *t*-test and Kruskal-Wallis test were used to test significance. **f**, The apical domain disassembles later in cells that express keratins. NEBD serves as reference to establish the time of apical domain disassembly.  $**P=0.0022$ ; two-tailed Mann-Whitney *U*-test. **g**, Scheme showing 2-cell stage injection strategy. Graphs show number of inner cells derived from non-injected cells versus cells injected with controls or treatments within the same 16-cell stage embryo.  $*P=0.0351$  (Par6b);  $*P=0.0322$  (Krt8 + Krt18 siRNA);  $**P=0.0036$  (Krt8 + Krt18 siRNA);  $**P=0.0043$  (Krt8 + Krt18 mRNA);  $***P=0.0002$ ; two-tailed Kruskal-Wallis test. **h**, Live imaging in intact embryos shows a representative example of a mitotic spindle losing its initial orthogonal orientation in an embryo microinjected with Krt8 + Krt18 siRNAs. Control cells maintain their initial orthogonal orientation, whereas Pard6b knockdown cells often fail to establish an orthogonal orientation. In box plots, the centre line is the median, box edges delineate upper and lower quartiles and whiskers represent the range. Scale bars, 10  $\mu$ m.

an apical MTOC. This relies on keratin expression, which differentially regulates cortex stability to support apical MTOC formation. Moreover, the timing of apical domain disassembly varies: in

cells expressing keratins, the apical domain is stabilized for longer. Yet, the apical domain is less stable without keratins and cells do not form an aster. PLK1 and katanin manipulations can enhance



or reduce the asymmetric features of the spindle. However, over-expression of PLK1(T210D)–Emerald is insufficient to change the proportion of cells assembling monoastral spindles. By contrast, forcing keratin expression increases the number of cells assembling monoastral spindles and also inner cell contribution. Thus, differential keratin expression explains why only a subset of cells establishes the monoastral spindle and produces inner progeny. Heterogeneities in keratin expression arise from transcriptional differences in the BAF chromatin remodelling complex at the 4-cell stage<sup>25,49</sup>. Therefore, our findings support a model whereby heterogeneities in the early embryo determine lineage patterning by differentially regulating (1) keratin expression, (2) stability of the apical cortex and timing of apical domain disassembly, and (3) establishment of a monoastral spindle that drives asymmetric cell divisions to segregate inner–outer cells and determine pluripotent–trophoblast fate (Extended Data Fig. 9).

We also reveal a non-stereotypical assembly pattern for the inter-polar parts of the spindle (Fig. 2). At earlier stages, spindles assemble from dispersed MTOCs following NEBD<sup>21,50,51</sup>. However, 8-cell blastomeres form a well-defined perinuclear MTOC. This difference may result from the developmental transition into a more polarized cellular architecture<sup>4</sup> or transcriptionally active cell states<sup>52</sup>. When the first spindle pole is coupled to the apical MTOC and aster, the rest of the spindle forms facing the basal cortex. Thus, the fully assembled spindle apparatus adopts a more orthogonal orientation. Furthermore, the apical pole sustains higher levels of PLK1 and microtubule growth than the basal. The retention of higher PLK1 levels and microtubule growth in the apical parts of the monoastral spindle may result from the differential distance to the apical cortex, as previous work<sup>53,54</sup> and our results here suggest that polarized regions of the cortex stimulate non-centrosomal MTOC function (Figs. 2 and 3). This may also explain why PLK1(T210D)–Emerald increases aster size in monoastral spindles, but not in anastral spindles, as their poles are further from the apical cortex.

We cannot dissect the exact contribution of the aster and inter-polar regions to the regulation of spindle angle. However, spindles not connected to the cortex typically align with the longest cell axis, consistent with Hertwig's rule<sup>55</sup>. By contrast, asters can facilitate alignments following orientations that do not follow this rule<sup>56–58</sup>. Unlike suggestions that inner cells can normally relocate from an inner to an outer position<sup>10</sup>, the more orthogonal patterns establish inner–outer segregation, as they enable the daughter positioned closer to the embryo's centre of mass to inherit a larger basolateral surface with more E-cadherin interactions. Consistently, we only detect repositioning of inner cells to the outer regions following E-cadherin disruption, but not in unperturbed embryos. In addition to biasing division angles, the monoastral spindle positions the cleavage furrow closer to the basal cortex, triggering differences in daughter volume. The smaller daughter contributes to the inner mass when the division plane is relatively orthogonal, but also in divisions where the smaller cell retains some surface exposed to the outer region and is internalized subsequently via apical constriction. The idea that smaller cells are more prone to internalization is supported by studies showing that *Drosophila* epithelial cells decrease their volume to trigger an increase in cortical tension and undergo internalization<sup>35</sup>. Furthermore, smaller cells have reduced apical surface area, which can concentrate myosin II to facilitate constriction<sup>3</sup>.

Finally, the apical and basal regions of the monoastral spindle and key microtubule regulators become asymmetrically inherited during division. This apical network may be supported by the inherited pool of PLK1 and Cdk5rap2 and other regulators such as CAMSAP proteins<sup>29</sup>. Importantly, these microtubules determine differential assembly of F-actin rings, apical polarization and Cdx2 expression. Differential actin ring regulation also contributes to inner–outer segregation, as the ring and its associated proteins

hinder apical constriction. However, our data suggest that outer cell position alone is insufficient to specify fate, as outer–outer daughters derived from katanin(S133G)-overexpressing cells display reduced Cdx2 expression, consistent with short spindles and the absence of F-actin rings.

Interestingly, the outer daughter derived from a cell with monoastral spindle is not only larger than the daughter that internalizes, but also larger than the two daughters derived from parental cells with anastral spindles. This cell also inherits a more extensive microtubule network and more Cdk5rap2 and PLK1–Emerald. The association between daughter volume and size of the inherited microtubule network may provide a scaling mechanism, whereby larger cells form F-actin rings with larger diameters. Similarly, outer–outer daughters derived from anastral spindles inherit smaller microtubule networks and form smaller rings, whereas inner cells from monoastral spindles do not inherit apical microtubules and do not form rings. Future studies should explore whether the asymmetric organization of the monoastral spindle provides additional ways to pattern cell lineages, which could rely on interactions with mRNAs<sup>59</sup>, organelles<sup>60</sup>, motor proteins<sup>29</sup> or chromatin regulators<sup>61</sup>.

### Online content

Any methods, additional references, Nature Research reporting summaries, source data, extended data, supplementary information, acknowledgements, peer review information; details of author contributions and competing interests; and statements of data and code availability are available at <https://doi.org/10.1038/s41556-021-00826-3>.

Received: 5 February 2021; Accepted: 30 November 2021;

Published online: 31 January 2022

### References

- Knoblich, J. A. Asymmetric cell division: recent developments and their implications for tumour biology. *Nat. Rev. Mol. Cell Biol.* **11**, 849–860 (2010).
- Johnson, M. H. & Ziomek, C. A. The foundation of two distinct cell lineages within the mouse morula. *Cell* **24**, 71–80 (1981).
- Samarage, C. R. et al. Cortical tension allocates the first inner cells of the mammalian embryo. *Dev. Cell* **34**, 435–447 (2015).
- Johnson, M. H. & Ziomek, C. A. Induction of polarity in mouse 8-cell blastomeres: specificity, geometry, and stability. *J. Cell Biol.* **91**, 303–308 (1981).
- Nishioka, N. et al. The Hippo signaling pathway components Lats and Yap pattern Tead4 activity to distinguish mouse trophoblast from inner cell mass. *Dev. Cell* **16**, 398–410 (2009).
- Hirate, Y. et al. Polarity-dependent distribution of angiominin localizes Hippo signaling in preimplantation embryos. *Curr. Biol.* **23**, 1181–1194 (2013).
- Leung, C. Y. & Zernicka-Goetz, M. Angiominin prevents pluripotent lineage differentiation in mouse embryos via Hippo pathway-dependent and -independent mechanisms. *Nat. Commun.* **4**, 2251 (2013).
- Cockburn, K., Biechele, S., Garner, J. & Rossant, J. The Hippo pathway member Nf2 is required for inner cell mass specification. *Curr. Biol.* **23**, 1195–1201 (2013).
- Lim, H. Y. G. & Plachta, N. Cytoskeletal control of early mammalian development. *Nat. Rev. Mol. Cell Biol.* **22**, 548–562 (2021).
- Watanabe, T., Biggins, J., Tannan, N. & Srinivas, S. Limited predictive value of blastomere angle of division in trophoblast and inner cell mass specification. *Development* **141**, 2279–2288 (2014).
- Maitre, J. L. et al. Asymmetric division of contractile domains couples cell positioning and fate specification. *Nature* **536**, 344–348 (2016).
- Niwayama, R. et al. A tug-of-war between cell shape and polarity controls division orientation to ensure robust patterning in the mouse blastocyst. *Dev. Cell* **51**, 564–574.e6 (2019).
- White, M. D. et al. Long-lived binding of Sox2 to DNA predicts cell fate in the four-cell mouse embryo. *Cell* **165**, 75–87 (2016).
- Torres-Padilla, M. E., Parfitt, D. E., Kouzarides, T. & Zernicka-Goetz, M. Histone arginine methylation regulates pluripotency in the early mouse embryo. *Nature* **445**, 214–218 (2007).
- Tabansky, I. et al. Developmental bias in cleavage-stage mouse blastomeres. *Curr. Biol.* **23**, 21–31 (2013).
- Goolam, M. et al. Heterogeneity in Oct4 and Sox2 targets biases cell fate in 4-cell mouse embryos. *Cell* **165**, 61–74 (2016).

17. Wang, J. et al. Asymmetric expression of LincGET biases in two-cell mouse embryos. *Cell* **175**, 1887–1901.e18 (2018).
18. Casser, E. et al. Totipotency segregates between the sister blastomeres of two-cell stage mouse embryos. *Sci. Rep.* **7**, 8299 (2017).
19. Grill, S. W. & Hyman, A. A. Spindle positioning by cortical pulling forces. *Dev. Cell* **8**, 461–465 (2005).
20. Gueth-Hallonet, C. et al.  $\gamma$ -Tubulin is present in acentriolar MTOCs during early mouse development. *J. Cell Sci.* **105**, 157–166 (1993).
21. Cliff, D. & Schuh, M. A three-step MTOC fragmentation mechanism facilitates bipolar spindle assembly in mouse oocytes. *Nat. Commun.* **6**, 7217 (2015).
22. Schatten, G., Simerly, C. & Schatten, H. Microtubule configurations during fertilization, mitosis, and early development in the mouse and the requirement for egg microtubule-mediated motility during mammalian fertilization. *Proc. Natl Acad. Sci. USA* **82**, 4152–4156 (1985).
23. Howe, K. & FitzHarris, G. A non-canonical mode of microtubule organization operates throughout pre-implantation development in mouse. *Cell Cycle* **12**, 1616–1624 (2013).
24. Korothevich, E. et al. The apical domain is required and sufficient for the first lineage segregation in the mouse embryo. *Dev. Cell* **40**, 235–247.e7 (2017).
25. Lim, H. Y. G. et al. Keratins are asymmetrically inherited fate determinants in the mammalian embryo. *Nature* **585**, 404–409 (2020).
26. Zenker, J. et al. Expanding actin rings zipper the mouse embryo for blastocyst formation. *Cell* **173**, 776–791.e17 (2018).
27. Tolic, I. M. Mitotic spindle: kinetochore fibers hold on tight to inter-polar bundles. *Eur. Biophys. J.* **47**, 191–203 (2018).
28. Colicino, E. G. & Hehnlly, H. Regulating a key mitotic regulator, polo-like kinase 1 (PLK1). *Cytoskeleton* **75**, 481–494 (2018).
29. Zenker, J. et al. A microtubule-organizing center directing intracellular transport in the early mouse embryo. *Science* **357**, 925–928 (2017).
30. Choi, Y. K., Liu, P., Sze, S. K., Dai, C. & Qi, R. Z. CDK5RAP2 stimulates microtubule nucleation by the gamma-tubulin ring complex. *J. Cell Biol.* **191**, 1089–1095 (2010).
31. Schulze, E., Asai, D. J., Bulinski, J. C. & Kirschner, M. Posttranslational modification and microtubule stability. *J. Cell Biol.* **105**, 2167–2177 (1987).
32. Dudka, D., Castrogiovanni, C., Liaudet, N., Vassal, H. & Meraldi, P. Spindle-length-dependent HURP localization allows centrosomes to control kinetochore–fiber plus-end dynamics. *Curr. Biol.* **29**, 3563–3578.e6 (2019).
33. Morris, S. A. et al. Origin and formation of the first two distinct cell types of the inner cell mass in the mouse embryo. *Proc. Natl Acad. Sci. USA* **107**, 6364–6369 (2010).
34. Rappaport, R. Cytokinesis in animal cells. *Int. Rev. Cytol.* **31**, 169–213 (1971).
35. Saias, L. et al. Decrease in cell volume generates contractile forces driving dorsal closure. *Dev. Cell* **33**, 611–621 (2015).
36. Lu, L. Y. et al. Polo-like kinase 1 is essential for early embryonic development and tumor suppression. *Mol. Cell Biol.* **28**, 6870–6876 (2008).
37. Jang, Y. J., Ma, S., Terada, Y. & Erikson, R. L. Phosphorylation of threonine 210 and the role of serine 137 in the regulation of mammalian polo-like kinase. *J. Biol. Chem.* **277**, 44115–44120 (2002).
38. McNally, F. J. & Vale, R. D. Identification of katanin, an ATPase that severs and disassembles stable microtubules. *Cell* **75**, 419–429 (1993).
39. Anani, S., Bhat, S., Honma-Yamanaka, N., Krawchuk, D. & Yamanaka, Y. Initiation of Hippo signaling is linked to polarity rather than to cell position in the pre-implantation mouse embryo. *Development* **141**, 2813–2824 (2014).
40. Feldman, J. L. & Priess, J. R. A role for the centrosome and PAR-3 in the hand-off of MTOC function during epithelial polarization. *Curr. Biol.* **22**, 575–582 (2012).
41. Alarcon, V. B. Cell polarity regulator PARD6B is essential for trophectoderm formation in the preimplantation mouse embryo. *Biol. Reprod.* **83**, 347–358 (2010).
42. Gard, D. L. Microtubule organization during maturation of *Xenopus* oocytes: assembly and rotation of the meiotic spindles. *Dev. Biol.* **151**, 516–530 (1992).
43. Schuh, M. & Ellenberg, J. Self-organization of MTOCs replaces centrosome function during acentrosomal spindle assembly in live mouse oocytes. *Cell* **130**, 484–498 (2007).
44. Mayer, T. U. et al. Small molecule inhibitor of mitotic spindle bipolarity identified in a phenotype-based screen. *Science* **286**, 971–974 (1999).
45. Ishii, R. & Shimizu, T. Equalization of unequal first cleavage in the Tubifex egg by introduction of an additional centrosome: implications for the absence of cortical mechanisms for mitotic spindle asymmetry. *Dev. Biol.* **189**, 49–56 (1997).
46. Ren, X. & Weisblat, D. A. Asymmetrization of first cleavage by transient disassembly of one spindle pole aster in the leech *Helobdella robusta*. *Dev. Biol.* **292**, 103–115 (2006).
47. Bergstrahl, D. T., Dawney, N. S. & St Johnston, D. Spindle orientation: a question of complex positioning. *Development* **144**, 1137–1145 (2017).
48. Bornens, M. Centrosome composition and microtubule anchoring mechanisms. *Curr. Opin. Cell Biol.* **14**, 25–34 (2002).
49. Panamarova, M. et al. The BAF chromatin remodelling complex is an epigenetic regulator of lineage specification in the early mouse embryo. *Development* **143**, 1271–1283 (2016).
50. Coelho, P. A. et al. Spindle formation in the mouse embryo requires Plk4 in the absence of centrioles. *Dev. Cell* **27**, 586–597 (2013).
51. Courtois, A., Schuh, M., Ellenberg, J. & Hiiragi, T. The transition from meiotic to mitotic spindle assembly is gradual during early mammalian development. *J. Cell Biol.* **198**, 357–370 (2012).
52. Schultz, R. M. Regulation of zygotic gene activation in the mouse. *Bioessays* **15**, 531–538 (1993).
53. Akera, T. et al. Spindle asymmetry drives non-Mendelian chromosome segregation. *Science* **358**, 668–672 (2017).
54. So, C. et al. A liquid-like spindle domain promotes acentrosomal spindle assembly in mammalian oocytes. *Science* **364**, eaat9557 (2019).
55. Hertwig, O. Das Problem der Befruchtung und der Isotropie des Eies, eine Theorie der Vererbung. *Enaische Z. Naturwissenschaft* **18**, 276–318 (1884).
56. Strauss, B., Adams, R. J. & Papalopulu, N. A default mechanism of spindle orientation based on cell shape is sufficient to generate cell fate diversity in polarised *Xenopus* blastomeres. *Development* **133**, 3883–3893 (2006).
57. Wyatt, T. P. et al. Emergence of homeostatic epithelial packing and stress dissipation through divisions oriented along the long cell axis. *Proc. Natl Acad. Sci. USA* **112**, 5726–5731 (2015).
58. Gray, D. et al. First cleavage of the mouse embryo responds to change in egg shape at fertilization. *Curr. Biol.* **14**, 397–405 (2004).
59. Skamagki, M., Wicher, K. B., Jedrusik, A., Ganguly, S. & Zernicka-Goetz, M. Asymmetric localization of Cdx2 mRNA during the first cell-fate decision in early mouse development. *Cell Rep.* **3**, 442–457 (2013).
60. Chi, F., Sharpley, M. S., Nagaraj, R., Roy, S. S. & Banerjee, U. Glycolysis-independent glucose metabolism distinguishes TE from ICM fate during mammalian embryogenesis. *Dev. Cell* **53**, 9–26.e4 (2020).
61. Ranjan, R., Snedeker, J. & Chen, X. Asymmetric centromeres differentially coordinate with mitotic machinery to ensure biased sister chromatid segregation in germline stem cells. *Cell Stem Cell* **25**, 666–681.e5 (2019).

**Publisher's note** Springer Nature remains neutral with regard to jurisdictional claims in published maps and institutional affiliations.

© The Author(s), under exclusive licence to Springer Nature Limited 2022

## Methods

**Mouse embryo work.** Superovulated wild-type female mice were used following animal ethics guidelines of the University of Pennsylvania. Embryos were flushed from oviducts with M2 medium (Merck) and cultured in KSOM+AA medium (Merck) at 37°C and 5% CO<sub>2</sub>, covered by mineral oil (Sigma). Live embryos were microinjected with 0.1 to 0.3 µl RNA in injection buffer (5 mM Tris, 5 mM NaCl, 0.1 mM EDTA) using a FemtoJet (Eppendorf).

For live imaging, embryos were cultured in LabTek chambers (Nunc) at 37°C and 5% CO<sub>2</sub> in an incubator adapted for the microscope system (Carl Zeiss LSM780, LSM880, ZEN Blue; Leica SP8, LAS-X 3.1.5). DNA constructs were cloned into pCS2+ vector for mRNA production. The mMACHINE mMACHINE SP6 kit (Ambion) was used to synthesize RNA using linearized plasmids as templates following manufacturer's instructions. RNA was purified using RNAeasy kit (Qiagen) following manufacturer's instructions. Embryos were microinjected with mRNA for EB3–Tomato, GFP–MAP2C and RFP–MAP2C and Cdk5rap2–Emerald at 100 ng µl<sup>-1</sup>; Utr–GFP, RFP–Utr at 40 ng µl<sup>-1</sup>; GFP–myosin II at 60 ng µl<sup>-1</sup>; H2B–RFP, H2B–GFP at 15 ng µl<sup>-1</sup>; Krt8 and Krt18–Emerald at 150 ng µl<sup>-1</sup>; Katanin(S133G) at 200 ng µl<sup>-1</sup>; PLK1(T210D)–Emerald, PLK1–Emerald at 100–200 ng µl<sup>-1</sup>; Lamin B1–Emerald 30 ng µl<sup>-1</sup> and RhoA(T19N) at 100 ng µl<sup>-1</sup>.

Embryos showing signs of abnormal or arrested development (~15%) were excluded following previous criteria<sup>62,63</sup>. We also previously demonstrated that embryos injected and imaged using similar conditions can generate viable offspring following transfer to pseudopregnant mice<sup>62</sup>. siRNAs (Qiagen) were microinjected, with a mock RNA, at 200–500 nM (Supplementary Table 1). Cytochalasin D was diluted in KSOM+AA medium and applied at 5 µg ml<sup>-1</sup> for 4 h before embryo fixation. Volasertib was diluted in KSOM+AA medium and applied after embryo compaction at 10 nM for the entire live-imaging experiment.

For immunolabelling, embryos were fixed in 4% paraformaldehyde in DPBS for 30 min at room temperature, washed in DPBS containing 0.1% Triton X-100, permeabilized for 30 min in DPBS containing 0.25% Triton X-100, incubated in blocking solution (10% fetal bovine serum in DPBS) for 2 h, incubated with antibodies for: α-tubulin (Sigma, T6199) at 1:500 and (GenTex, GTX109832), 1:400; PLK1 (Thermo Scientific, 35–206), at 1:200; HURP (Atlas antibodies, HPA005546), at 1:200; polyglutamylated tubulin (Sigma, T9822), at 1:200; tyrosine tubulin (Sigma, T9028), 1:200; or γ-tubulin (Sigma, T3559), 1:500—in blocking solution overnight at 4°C, rinsed in DPBS, incubated with secondary Alexa Fluor 488-conjugated antibody (Invitrogen) in blocking solution (1:500) for 2 h and rinsed in DPBS. To label F-actin, fixed embryos were incubated with Phalloidin–Rhodamine (Molecular Probes, R415) at 1:500 and for nuclear staining with DAPI (Sigma, 10236276001) at 1:1,000. To block E-cadherin function, embryos were treated with the DECMA1 antibody (Sigma, U3254) or control IgG antibody (Sigma) at 1:200 in KSOM+AA medium.

Quantitative PCR with reverse transcription (RT–qPCR) was performed using a TaqManAR RNA-to-CT 1-Step Kit (Applied Biosystems) and Lightcycler 480II qPCR (Roche) with the following primer pairs: *Katn1*: forward, 5'-AAATTGGCTCGTGAATATGCACT-3', reverse, 5'-CGGAGGTGTGTATCTTTGACTG-3'; *Gapdh*: forward, 5'-CATGGCCTCCGGTGTCTCA-3', reverse, 5'-TACTTGGCAGGTTTCTCCAGG-3'.

**Live-embryo imaging.** Live embryos were imaged using a laser-scanning confocal microscope (Zeiss LSM 780, Zeiss LSM 800, Zeiss LSM880 and Leica SP8) with water Apochromat 40× 1.1 NA objectives and highly sensitive avalanche photodiode light detectors of the Confocor 3 module (Zeiss), Airyscan (Zeiss) and HyD detectors (Leica).

**Image analysis.** Three-dimensional visualizations of embryos were performed using Imaris 8.2 software (Bitplane). The manual surface rendering module was used for cell segmentation. Cell volume was derived from the segmented data using the Imaris statistics module. Ring perimeter was measured using Imaris point measurement tool. The ring width was measured as the mean distance between the ring's borders for ten different positions using Imaris point measurement tool. The distance from the centre of mass of the cell to the apical membrane was calculated using segmented data in Imaris. Quantification of immunofluorescence intensity and expression levels were performed in Imaris and Fiji by measuring mean fluorescence intensity at a region of interest (ROI). Spindle orientation was measured by calculating the angle between the pole-to-DNA and DNA-to-embryo's centre in Imaris. Spindle length was measured at the end of metaphase. Monoastral spindles were identified by their asymmetry and in immunofluorescence images also by the presence of monopolar asters. Microtubule density in the growing spindle was measured using the intensity profile tool in ZEN Blue or Fiji. For inner cell quantification, one cell of a two-cell-stage embryo was injected with mRNAs and/or siRNAs, and the embryos were allowed to develop to the 16-cell stage.

**Microtubule density between spindle pole and cell cortex.** Surface of rendered aster was created as described in Extended Data Fig. 5g and intensity was analysed with Imaris.

**Spindle intensity ratio analysis.** Fluorescence intensity ratio between the apical and basal sides of the spindles was calculated using segmented data in Imaris, corrected by background fluorescence:

$$I_r = (I_{Ra} \times I_{Bb}) / (I_{Rb} \times I_{Ba})$$

Where  $I_{Ra}$  and  $I_{Rb}$  are fluorescence intensity divided by volume within apical or basal ROIs, respectively.  $I_{Ba}$  and  $I_{Bb}$  are averages of fluorescence intensity divided by volume within four non-ROIs at the same focal plane as  $I_{Ra}$  or  $I_{Rb}$ , respectively, within the same cell.

**EB3–Tomato tracking.** The Imaris manual spot-detection module was used to analyse EB3–Tomato tracks. Only comets detected in at least four continuous time frames were used for analysis. Comets moving along the z-axis were excluded from analysis. The number of EB3–Tomato-labelled tracks was scored within 1 min in a ROI in the vicinity of the spindle pole.

**Statistical analysis and reproducibility.** Statistical analyses were performed in Excel and GraphPad Prism. Data were analysed for normality using a D'Agostino–Pearson omnibus normality test. Variables displaying a normal distribution were analysed using an unpaired, two-tailed Student's *t*-test for two groups, or Kruskal–Wallis test with Kruskal–Wallis test for two groups or more than two groups, respectively. Variables that did not follow a normal distribution were analysed using an unpaired, two-tailed Mann–Whitney *U*-test for two groups, and Kruskal–Wallis test with Dunn's multiple comparisons test for more than two groups. Reproducibility was confirmed by independent experiments.

Data in Fig. 3a,b are from seven and six independent experiments, respectively. Data in Fig. 4c are from five independent experiments. Data in Fig. 4a are from three independent experiments. Data for each condition in Fig. 4e are from three to eight independent experiments as follows: Scramble Mono and Ana, eight; PLK1 siRNA, six; PLK1 WT Mono and Ana, three; PLK1(T210D) Mono and Ana, five. Data for each condition in Fig. 4j are from three to six independent experiments as follow: Scramble Mono and Ana, six; Katanin(S133G), three; Katanin siRNA Mono and Ana, six. Data in Fig. 5a,b are from four and three independent experiments, respectively. Data in Fig. 7a,b are from seven independent experiments. Data in Fig. 7c,h are from five and three independent experiments, respectively. Data in Extended Data Fig. 2c,j,h and Extended Data Fig. 2n, left, are from three independent experiments. Data in Extended Data Fig. 2f,g are from four independent experiments. Data in Extended Data Fig. 2a,b,d,e,i,k,l and Extended Data Fig. 2n, right are from seven independent experiments. Data in Extended Data Fig. 5b are from three independent experiments for each treatment. Data for each condition in Extended Data Fig. 5h are from three to five independent experiments as follows: Control, five; Volasertib, three; PLK1(T210)–Emerald, five; PLK1 siRNA, four; Katanin(S133G) and siRNA, three. Data in Extended Data Fig. 5m are from three (katanin(S133G) and siRNA) to five (control) independent experiments. Data in Extended Data Fig. 5g are from 43 independent experiments for various treatments. Data in Extended Data Fig. 6a–d are from five, six, five and four independent experiments, respectively. Data in Extended Data Fig. 7a,b are from three independent experiments. Data in Extended Data Fig. 8a–c,e are from three, four, four and three independent experiments, respectively.

**Reporting Summary.** Further information on research design is available in the Nature Research Reporting Summary linked to this article.

## Data availability

Source data are provided with this paper. All data supporting the findings of this study are available from the corresponding author on reasonable request. Source data are provided with this paper.

## References

- Kaur, G. et al. Probing transcription factor diffusion dynamics in the living mammalian embryo with photoactivatable fluorescence correlation spectroscopy. *Nat. Commun.* **4**, 1637 (2013).
- Fierro-Gonzalez, J. C., White, M. R., Silva, J. & Plachta, N. Cadherin-dependent filopodia control preimplantation embryo compaction. *Nat. Cell Biol.* **15**, 1424–1433 (2013).
- Loughlin, R., Wilbur, J. D., McNally, F. J., Nedelec, F. J. & Heald, R. Katanin contributes to interspecies spindle length scaling in *Xenopus*. *Cell* **147**, 1397–1407 (2011).

## Acknowledgements

This work was supported by grants from the National Institutes of Health: National Institute of General Medical Sciences (GM139970-01) and Eunice Kennedy Shriver National Institute of Child Health and Human Development (HD102013-01A1).

**Author contributions**

O.P. conceived the project, performed the experiments and data analysis and wrote the manuscript with contributions from all other authors. H.Y.G.L., R.M.S. and A.A.M. assisted with experiments and data analysis. P.T. and S.B. performed mouse work and embryo microinjection experiments. N.P. supervised the project.

**Competing interests**

The authors declare no competing interests.

**Additional information**

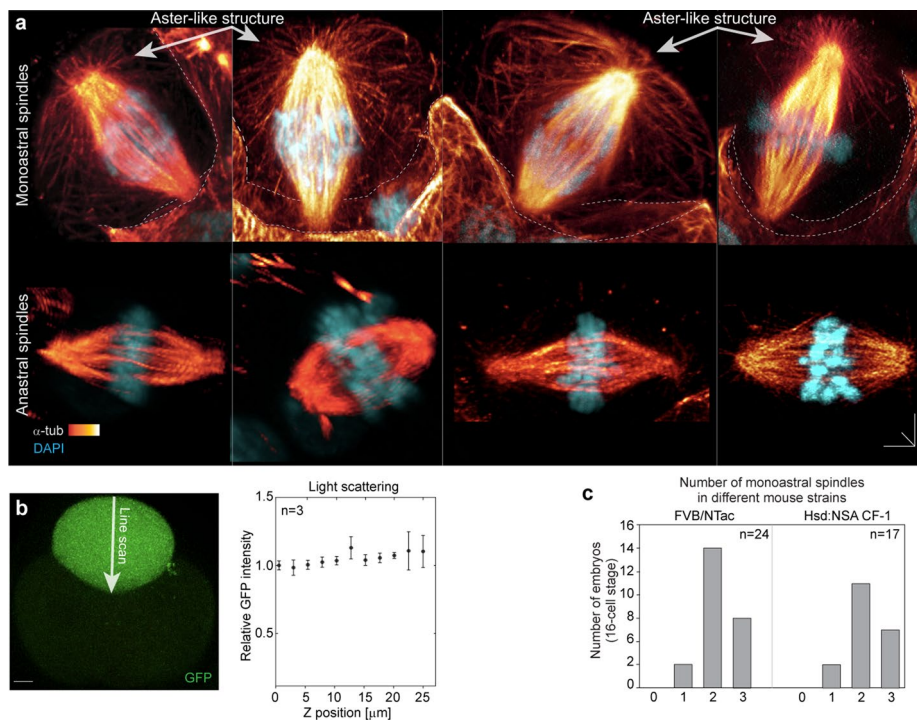
**Extended data** is available for this paper at <https://doi.org/10.1038/s41556-021-00826-3>.

**Supplementary information** The online version contains supplementary material available at <https://doi.org/10.1038/s41556-021-00826-3>.

**Correspondence and requests for materials** should be addressed to Nicolas Plachta.

**Peer review information** *Nature Cell Biology* thanks William Bement, Marta Shahbazi and the other, anonymous reviewer(s) for their contribution to the peer review of this work.

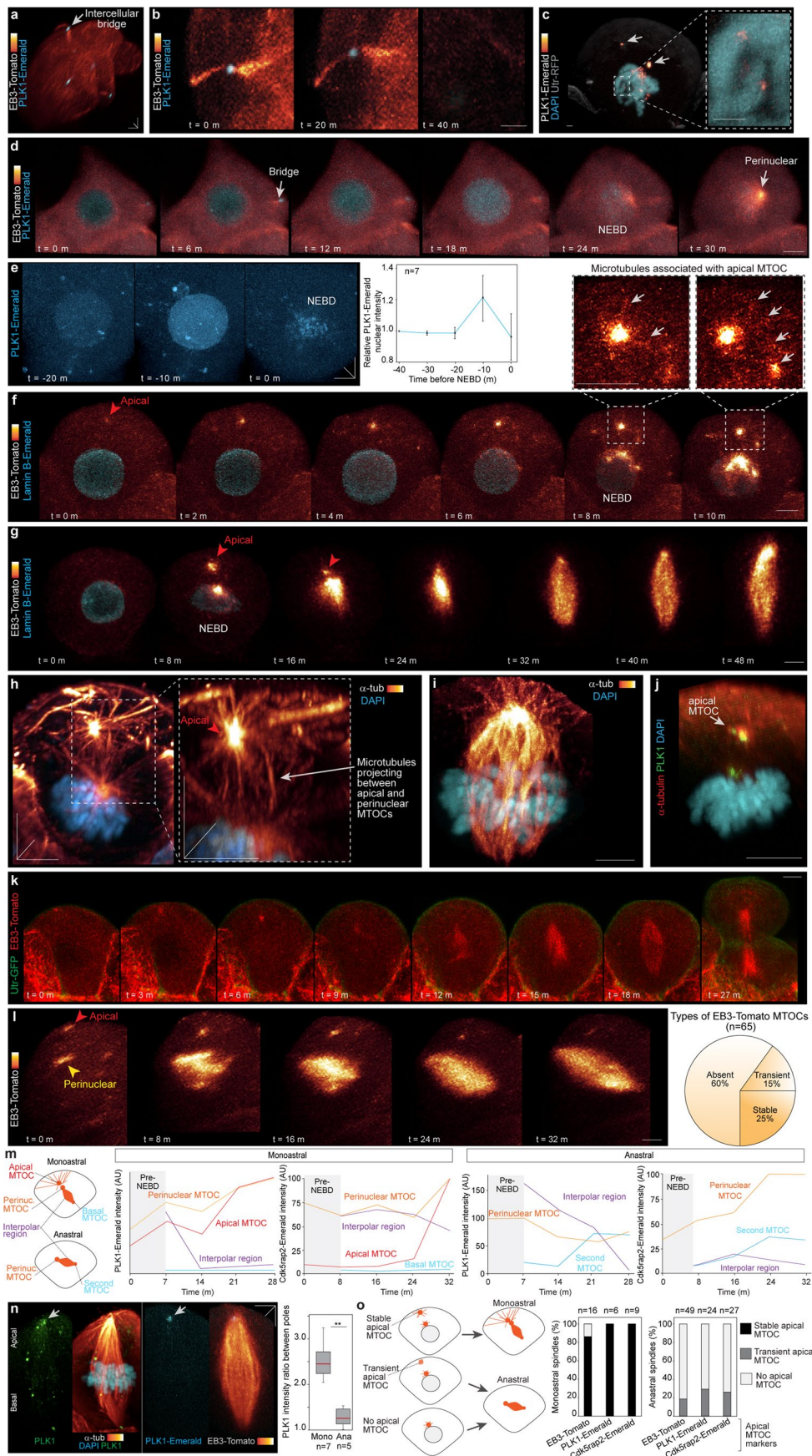
**Reprints and permissions information** is available at [www.nature.com/reprints](http://www.nature.com/reprints).



**Extended Data Fig. 1 | Additional characterization of the monoastral mitotic spindle. a**, Additional examples of 8- to 16-cell stage mouse embryos displaying monoastral and anastral mitotic spindles. Dashed lines mark cortical microtubules. Data are from seven independent experiments.

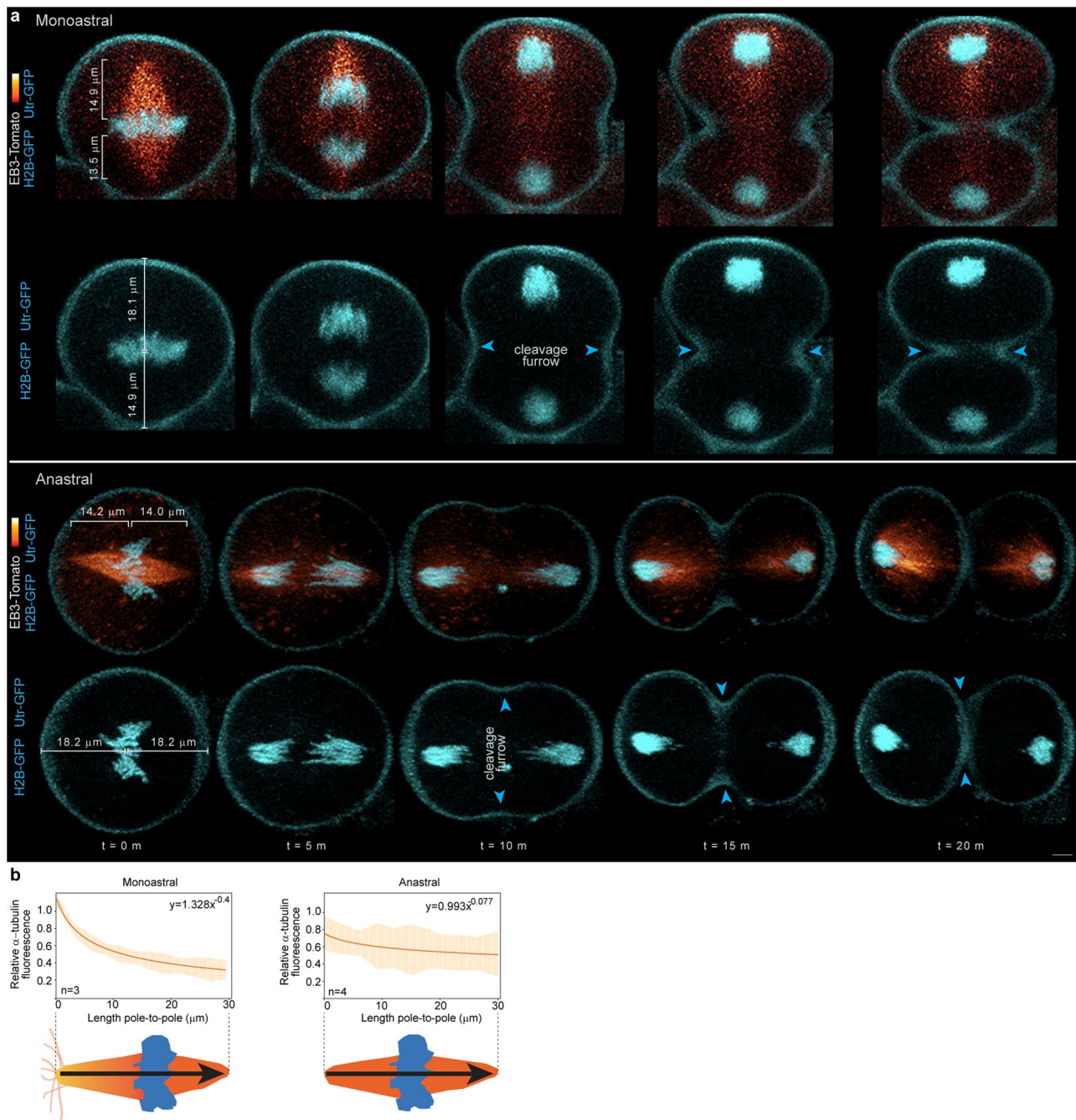
**b**, Light-scattering measurements in embryos injected with GFP mRNA at the 2-cell stage and imaged during the 8- to 16-cell stage. Quantification of GFP fluorescence along the axial (z) axis reveals no light scattering along the entire depth of a cell. Error bars represent s.e.m. Data are from three independent experiments.

**c**, Monoastral spindles frequency is similar in different genetic backgrounds ( $p = 0.99$  by Kolmogorov-Smirnov test). Scale bars,  $5 \mu\text{m}$  in xyz.

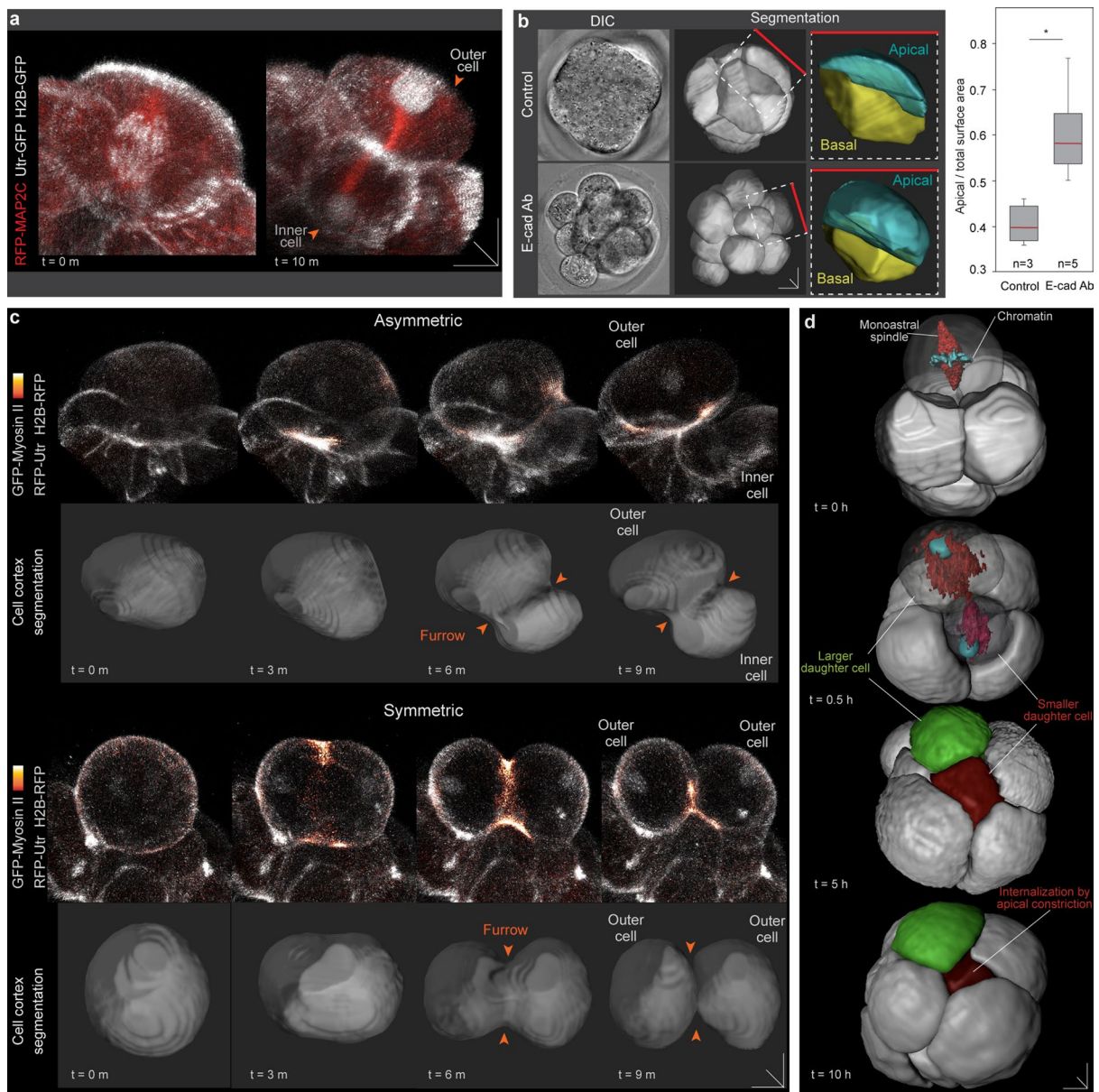


Extended Data Fig. 2 | See next page for caption.

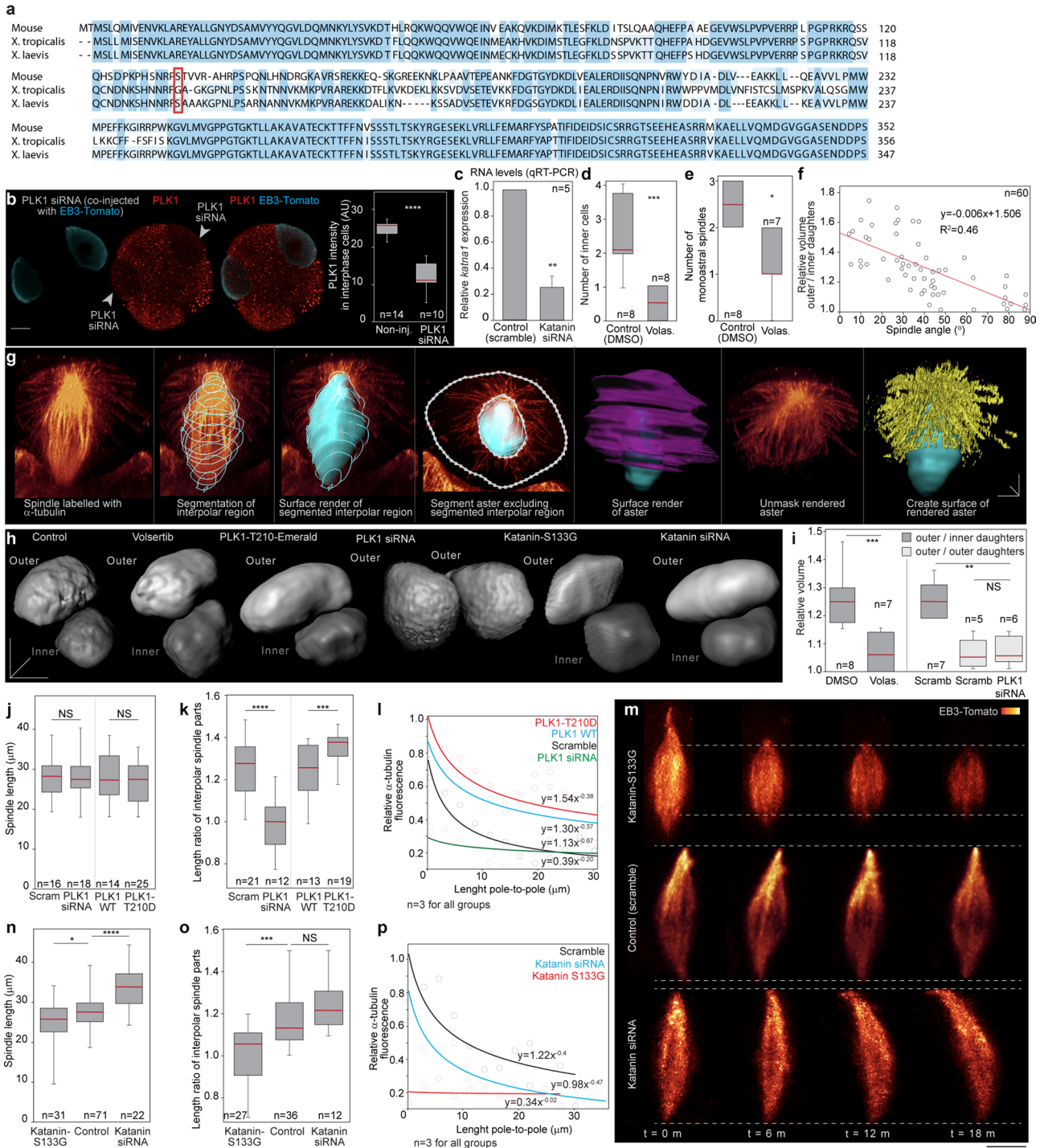
**Extended Data Fig. 2 | Additional characterization of PLK1 and spindle assembly dynamics.** **a,b**, Live embryos show localization of PLK1-Emerald to the bridges, connecting sister cells, during interphase (**b**), and disappearance from the bridge prior to mitosis (**b**). **c**, Consistent with its localization on kinetochores from late prophase, PLK1-Emerald puncta are visualized at chromosomes (inset). Bona fide apical and perinuclear PLK1-Emerald-positive MTOCs are also visualized (arrows). **d**, Live-imaging shows the dynamics of PLK1-localization at the intercellular bridge, cell nucleus and forming spindle. **e**, Live imaging and graph show that PLK1-Emerald is enriched in the nucleus before NEBD. **f**, Live-imaging shows that the onset of microtubule growth from the apical and perinuclear MTOCs of the monoastral spindle corresponds with the timing of NEBD. The apical MTOC starts to assemble the astral array (arrows), while the perinuclear MTOC starts to assemble the first spindle half of the future interpolar parts of the spindle. **g**, Following NEBD, the two main MTOCs that form the monoastral mitotic spindle are moving closer. **h, i**, Immunofluorescence in non-injected 8-cell embryos. At prophase, microtubules are projected between the apical and perinuclear MTOCs (**h**) to assemble the monoastral spindle (**i**). **j**, Localization pattern of endogenous PLK1 at the monoastral mitotic spindle. **k**, Live-imaging. In these focal planes, only the apical MTOC is initially visible. Note how the apical MTOC joins the rest of the mitotic spindle. **l**, Live-imaging during the assembly of an anastral mitotic spindle. In some cases of anastral spindle assembly, an apical EB3-Tomato-positive structure is initially detected, but this fails to display significant microtubule growth and to join the rest mitotic spindle apparatus. Graph shows the proportion of cells displaying this behavior. **m**, Quantification of PLK1-Emerald and Cdk5rap2-Emerald fluorescence intensities at the main parts of the monoastral and anastral mitotic spindles. Note the retention of high fluorescence levels in the apical parts of the monoastral spindle. **n**, Immunostaining and live imaging of PLK1 and microtubules and quantification of PLK1 intensity ratio between the apical and the basal poles (arrow shows apical pole). In box plot, centre line is the median, box edges show upper and lower quartiles and whiskers represent the range.  $**p = 0.0025$ ; Two-tailed Mann-Whitney *U*-test. **o**, Quantification of apical MTOC stability in monoastral and anastral spindles. Scale bars, 10  $\mu\text{m}$  in **a,b, d-l, n**; 2  $\mu\text{m}$  in **c**. Source numerical data are provided in source data.



**Extended Data Fig. 3 | Additional characterization of the asymmetric organization of the monoastral spindle. a**, Selected time-frames from live-imaging experiments performed in whole 8-cell embryos comparing the different division pattern of a cell with an original monoastral or anastral mitotic spindle. Data are from six independent experiments. **b**, Scheme and quantification of the variability in  $\alpha$ -tubulin fluorescence intensity from pole-to-pole along monoastral and anastral spindles. Scale bars, 5  $\mu\text{m}$ . Source numerical data are provided in source data.

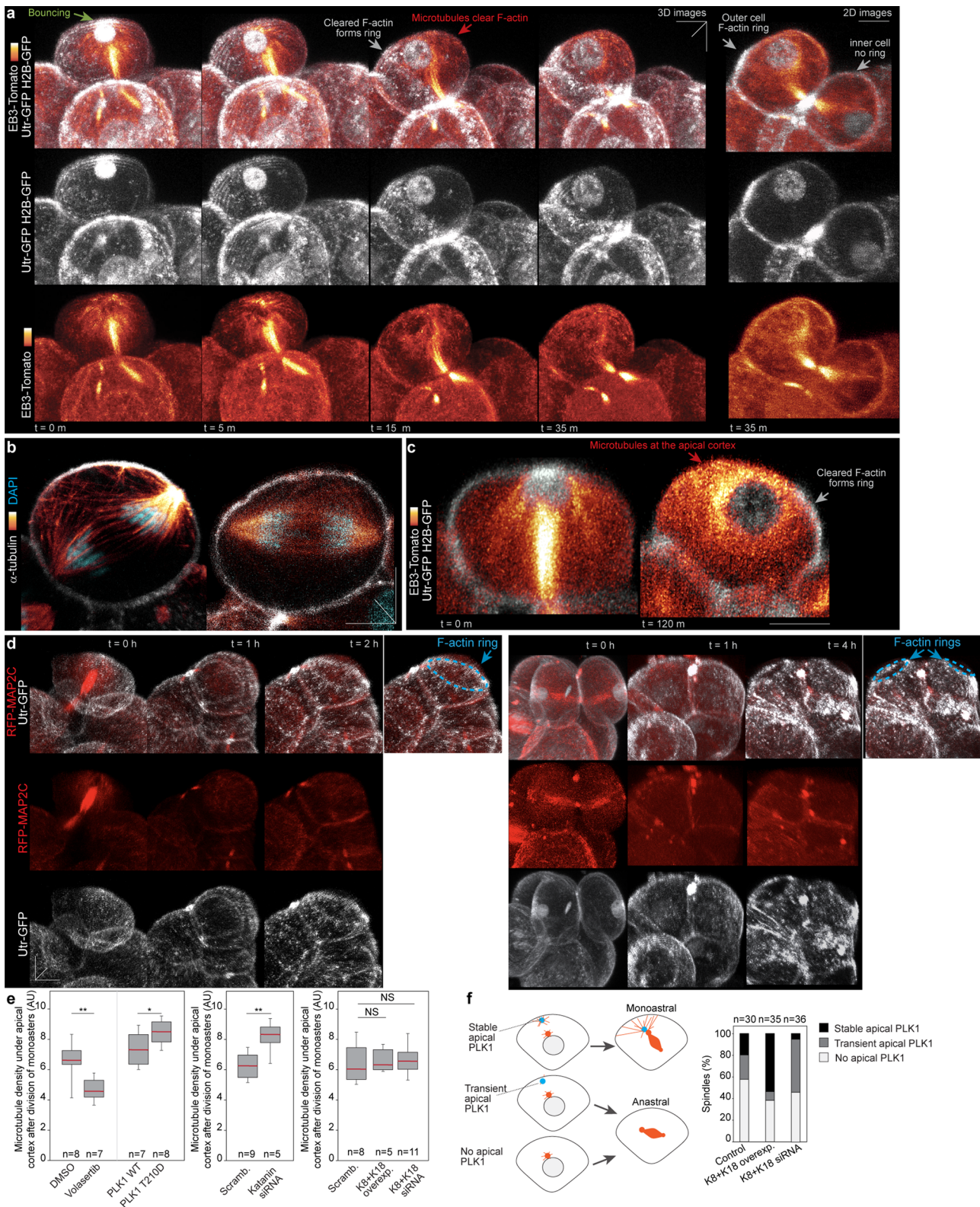


**Extended Data Fig. 4 | Additional characterization of asymmetric cell division pattern in cells with monoastral spindles. a**, Live-imaging of a cell undergoing asymmetric cell division. Data are from seven independent experiments. **b**, Disruption of E-cadherin trans interactions using acute treatment with the DECMA1 antibody pushes cells to adopt more outer positions displaying a larger apical than basal surface area.  $*p = 0.0357$ ; Unpaired two-tailed Mann Whitney  $U$ -test. In box plot, the centre line is the median, box edges show upper and lower quartiles and whiskers represent the range. Data are from three independent experiments. **c**, Live-imaging of GFP-myosin II together with RFP-Utr and H2B-RFP marker reveal two main modes of cell in the intact 8-cell embryo. In some cases, GFP-myosin II accumulates asymmetrically at the cell cortex, closer to the basal region. This corresponds with a more orthogonal division angle and differences in outer-inner cell volumes, similar to cells with monoastral mitotic spindles. Conversely, in some cases, GFP-myosin II accumulates more symmetrically at the cell equator. This is followed by more symmetric division patterns and outer-outer daughter volumes, similar to cells with anastral spindles. Data are from five independent experiments. **d**, Example of computer segmentation analysis used to track spindle types, division patterns and cell position. Monoastral spindles are detectable by their larger apical than basal regions and their asymmetry in microtubule intensities and orthogonal orientations. Note that with this resolution, the thinner astral microtubule array is not computationally segmented and is thus not visible. Cell tracking permits to follow the more asymmetric division pattern of this cell. Note the asymmetries between the two daughter cells in the inheritance of microtubules associated with the spindle of the parental cell and their final position. Data are from six independent experiments. Scale bars, 10  $\mu$ m. Source numerical data are provided in source data.



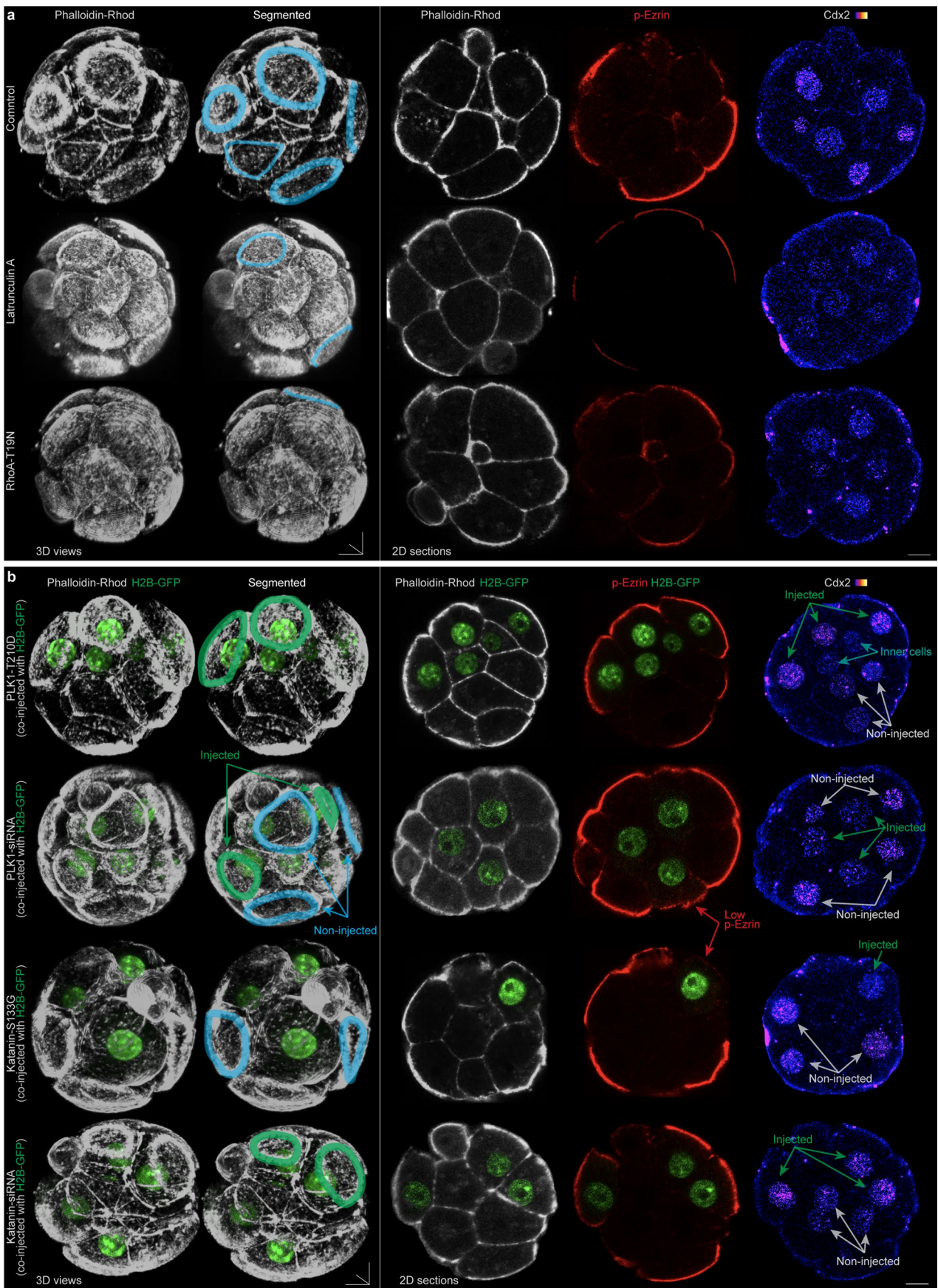
Extended Data Fig. 5 | See next page for caption.

**Extended Data Fig. 5 | Additional characterization of spindle manipulations.** **a**, Protein sequence comparison between mouse katanin, *Xenopus tropicalis*, and *Xenopus laevis* sequences. Phosphorylation site serine 131, which inhibits katanin activity, is found in *X. laevis* but missing from *X. tropicalis*. Mouse katanin has this phosphorylation site at serine 133 (marked in red). In line with *Xenopus* experiments<sup>64</sup>, elimination of the phosphorylation site (katanin-S133G) decreases spindle length. Only a portion of the protein sequences is shown. **b**, Immunofluorescence for PLK1 in an 8-cell embryo injected into one cell of the 2-cell stage with PLK1 siRNAs and EB3-Tomato. Cyan fluorescence shows injected cells. The image shows a thin confocal section (10  $\mu\text{m}$  thickness) scanned with high laser power to reveal differences in PLK1 levels between non-injected and injected cells at the same focal planes. Graph shows reduction of PLK1 intensity in the injected cells (Mann Whitney *U*-test). **c**, Microinjection of *Katna1* siRNAs reduces the expression of katanin p60 mRNA, quantified by qPCR in 16-cell embryo homogenates. **d,e**, Embryos treated with PLK1-inhibitor volasertib produce fewer inner-cells (Mann Whitney *U*-test) (**d**), and produce fewer monoastral spindles. **f**, Correlation between spindle angles (metaphase) and relative volumes of daughter cells (telophase). **g**, Step-by-step protocol used to segment microtubule asters and interpolar regions of the mitotic spindles (related to Figs. 1d and 4g,i). **h**, Computer segmentation of inner and outer daughter cells after division shows the effect of PLK1 and katanin manipulations on cell volume. **i**, Relative daughter cell volumes after manipulations of PLK1 (Mann Whitney *U*-test and Kruskal-Wallis). **j, n**, Spindle length after PLK1 and katanin manipulations. Mann Whitney *U*-test (**j**) and Kruskal-Wallis test (**n**). NS, not significant. **k, o**, Length ratio between the two interpolar parts of the spindle after PLK1 and katanin manipulations. Mann Whitney *U*-test (**k**) and Kruskal-Wallis test (**o**). **l, p**, Quantifications of the variability in  $\alpha$ -tubulin fluorescence intensity from pole-to-pole along spindles after PLK1 and katanin manipulations (see scheme in Extended Data Fig. 3b). **m**, Examples of mitotic spindles in live embryos following katanin manipulations. Scale bars, 10  $\mu\text{m}$  in **b,h,m**; 3  $\mu\text{m}$  in **g**. Source numerical data are provided in source data.



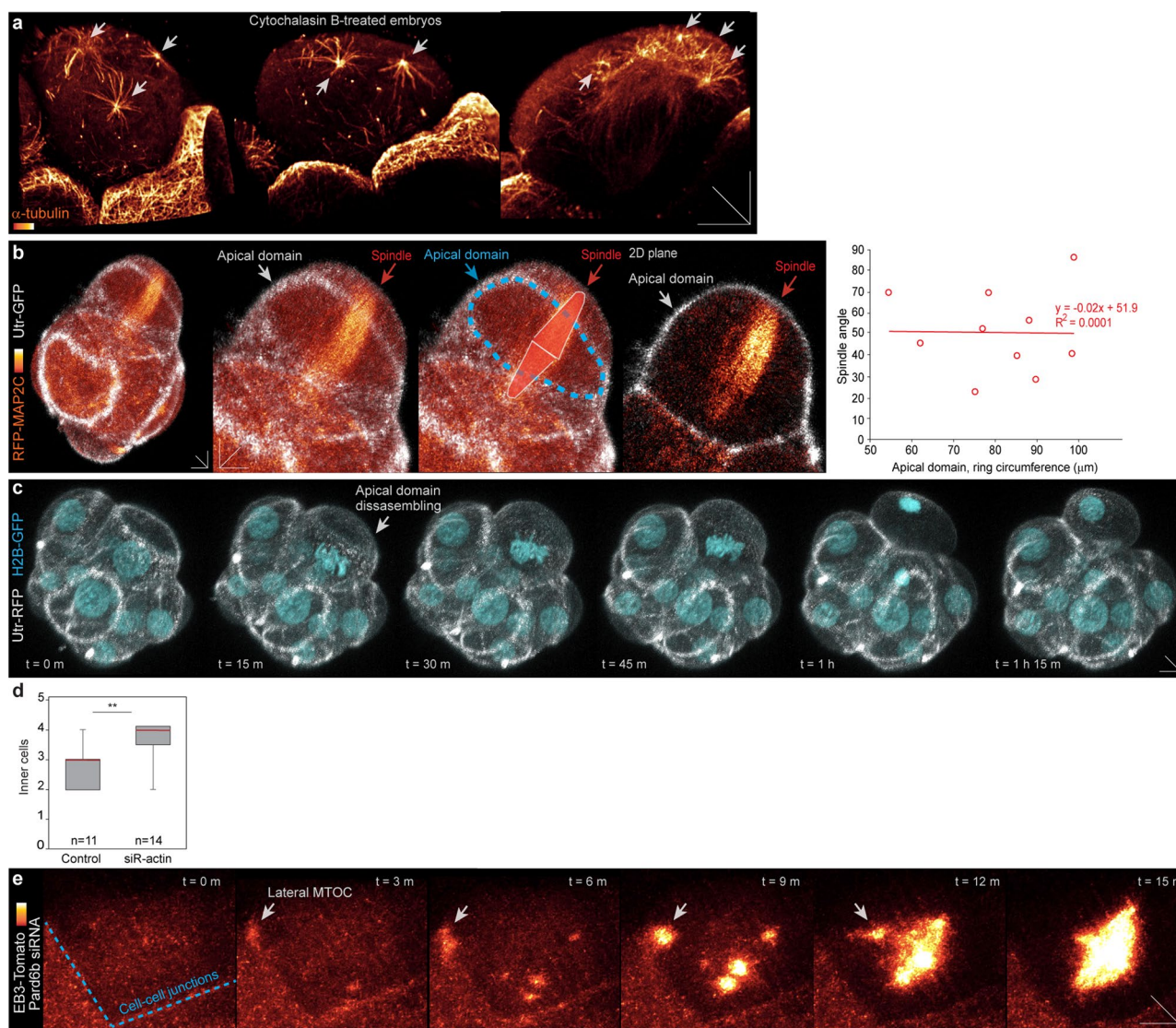
Extended Data Fig. 6 | See next page for caption.

**Extended Data Fig. 6 | Additional characterization of F-actin ring formation by asymmetric inheritance of microtubules.** **a**, Live-imaging of EB3-Tomato, Ezrin-GFP and H2B-GFP shows F-actin clearance by microtubules in an outer cell after division. **b**, Staining for  $\alpha$ -tubulin, Phalloidin-Rhodamine and DAPI in non-injected 8-cell embryos. Left panel shows additional example of a cell undergoing division. A more extensive microtubule network is present on the apical side. **c**, Live-imaging shows retention of microtubules at the apical cortex of the outer cell during interphase. **d**, Live-imaging for RFP-MAP2C and Utr-GFP shows examples of F-actin ring formation in outer cells derived from monoastral (left panels) and anastral spindles (right panels). The outer cell derived from the monoastral spindle forms a ring which is larger than those formed by the two outer daughters derived from the anastral spindle. **e**, Microtubule density under the apical cortex in daughter cells derived from parental cells with monoastral or anastral spindles, quantified two hours after division. Right panels show the effect of PLK1 and katanin manipulations. In box plots, the centre line is the median, box edges show upper and lower quartiles and whiskers represent the range.  $*p = 0.0499$ ,  $**p = 0.0059$  for volasertib,  $**p = 0.007$  for katanin; Two-tailed Mann Whitney *U*-test and Kruskal-Wallis test were used to test significance. **f**, Scheme and quantification of apical PLK1 stability after keratin manipulations. Scale bars, 10  $\mu\text{m}$ . Source numerical data are provided in source data.

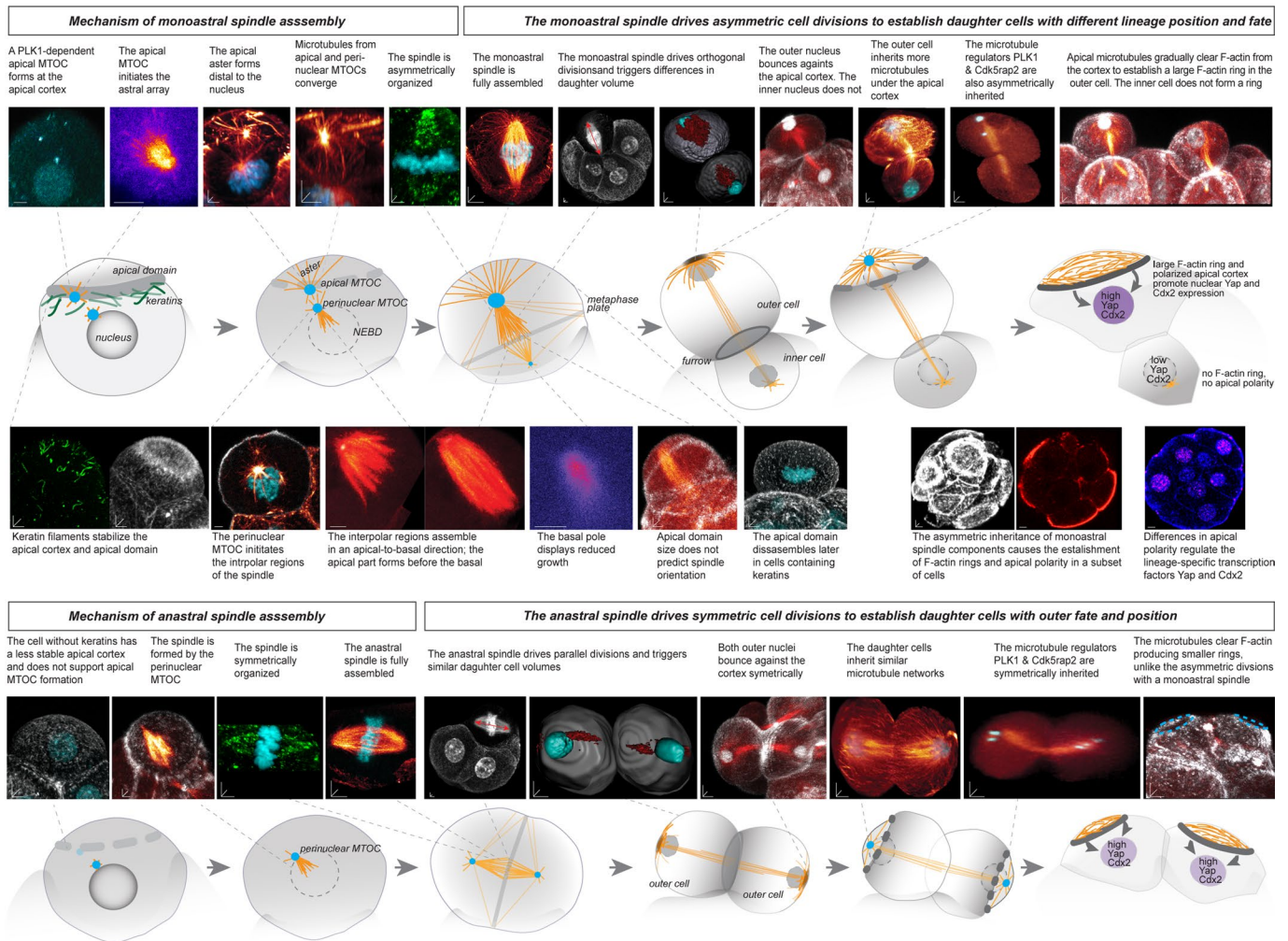


Extended Data Fig. 7 | See next page for caption.

**Extended Data Fig. 7 | Spindle manipulations affect F-actin ring formation, apical polarization and Cdx2 levels.** **a**, Embryos treated with Latrunculin A or microinjected at the 1-cell stage with RhoA-T19N display smaller F-actin rings assessed by Phalloidin-Rhodamine staining, lower apical polarization assessed by antibodies against phospho-Ezrin and lower Cdx2 levels. In the segmented 3D views, the F-actin rings have been computationally traced to highlight their size. The embryos were fixed at the 16-cell stage. **b**, Embryos microinjected into one cell at the 2-cell stage and fixed at the 16-cell stage show the effects of PLK1 and katanin manipulation on F-actin rings, Phospho-Ezrin and Cdx2 levels. Scale bars, 10  $\mu\text{m}$ .



**Extended Data Fig. 8 | Additional characterization of spindle and ring formation.** **a**, Immunofluorescence for  $\alpha$ -tubulin in embryos treated with Cytochalasin D. Disruption of the cortical actin by drug treatment triggers the formation of multiple ectopic MTOCs. **b**, Live-imaging of Utr-GFP and RFP-MAP2C in intact embryo shows a lack of correlation between the apical domain's size and the orientation of the mitotic spindle. Note how the apical spindle pole does not preferentially target the border of the apical domain. Moreover, the spindle shown is aligned relatively orthogonal in a cell displaying a larger apical domain. This contrasts with models suggesting that a small apical domain determines orthogonal spindle positioning. **c**, Live-imaging of RFP-Utr and H2B-GFP in an intact embryo shows an additional example of apical domains disassembly during mitosis. **d**, Graph shows the number of inner-cells in the 16-cell stage embryos. Embryos treated with SiR-actin produce more inner-cells than controls. The centre line is the median, box edges show upper and lower quartiles and whiskers represent the range.  $**p = 0.0019$ ; Two-tailed Mann Whitney *U*-test was used to test significance. **e**, Live-imaging of EB3-Tomato injected with Pard6b siRNA. Note that distal-MTOC origin from the cell-cell junctions (lateral MTOC) instead of the apical cortex, compared to Fig. 2c and Extended Data Fig. 2f,g,k. Scale bars, 10  $\mu$ m. Source numerical data are provided in source data.



**Extended Data Fig. 9 | Summary of main findings.** Schematic model shows the central steps by which cells assemble monoastral and anastral spindles, and how spindle organization determines division patterns and inner-outer lineage fate. Smaller insets highlight the main results supporting the model. Scale bars, 5  $\mu\text{m}$ .

## Reporting Summary

Nature Research wishes to improve the reproducibility of the work that we publish. This form provides structure for consistency and transparency in reporting. For further information on Nature Research policies, see [Authors & Referees](#) and the [Editorial Policy Checklist](#).

### Statistics

For all statistical analyses, confirm that the following items are present in the figure legend, table legend, main text, or Methods section.

n/a Confirmed

- The exact sample size ( $n$ ) for each experimental group/condition, given as a discrete number and unit of measurement
- A statement on whether measurements were taken from distinct samples or whether the same sample was measured repeatedly
- The statistical test(s) used AND whether they are one- or two-sided  
*Only common tests should be described solely by name; describe more complex techniques in the Methods section.*
- A description of all covariates tested
- A description of any assumptions or corrections, such as tests of normality and adjustment for multiple comparisons
- A full description of the statistical parameters including central tendency (e.g. means) or other basic estimates (e.g. regression coefficient) AND variation (e.g. standard deviation) or associated estimates of uncertainty (e.g. confidence intervals)
- For null hypothesis testing, the test statistic (e.g.  $F$ ,  $t$ ,  $r$ ) with confidence intervals, effect sizes, degrees of freedom and  $P$  value noted  
*Give  $P$  values as exact values whenever suitable.*
- For Bayesian analysis, information on the choice of priors and Markov chain Monte Carlo settings
- For hierarchical and complex designs, identification of the appropriate level for tests and full reporting of outcomes
- Estimates of effect sizes (e.g. Cohen's  $d$ , Pearson's  $r$ ), indicating how they were calculated

*Our web collection on [statistics for biologists](#) contains articles on many of the points above.*

### Software and code

Policy information about [availability of computer code](#)

Data collection

Time-lapse imaging of live samples and single confocal scans of fixed immunostained samples were both performed using Zeiss ZEN software, on a Zeiss LSM 780, LSM 800 or LSM 880 and using LAS-X 3.1.5 software, on Leica SP8.

Data analysis

All image analyses were performed using Imaris 8.2 (Bitplane AG) and ImageJ-Win64 Fiji. Statistical analyses were performed using GraphPad Prism (Version 8.3) and Microsoft Excel (Version 16.3).

For manuscripts utilizing custom algorithms or software that are central to the research but not yet described in published literature, software must be made available to editors/reviewers. We strongly encourage code deposition in a community repository (e.g. GitHub). See the Nature Research [guidelines for submitting code & software](#) for further information.

### Data

Policy information about [availability of data](#)

All manuscripts must include a [data availability statement](#). This statement should provide the following information, where applicable:

- Accession codes, unique identifiers, or web links for publicly available datasets
- A list of figures that have associated raw data
- A description of any restrictions on data availability

Source Data behind Figs. 1 to 7 and Extended Data Figs. 1 to 9 are available within the manuscript files.

### Field-specific reporting

Please select the one below that is the best fit for your research. If you are not sure, read the appropriate sections before making your selection.

- Life sciences       Behavioural & social sciences       Ecological, evolutionary & environmental sciences

## Life sciences study design

All studies must disclose on these points even when the disclosure is negative.

Sample size	No statistical test was performed to determine sample size. Sample size was determined based on prior experience and typical ranges used by research groups in the preimplantation mouse embryo field, and also in accordance to statistical test requirements. Previous work utilizing similar sample sizes includes Zenker et al. 2018 Cell 173:776-791; Zenker et al. 2017 Science 357: 925-928; White et al. 2016 Cell 165(1): 75-87; Lim et al. 2020 Nature 585(7825):404-409
Data exclusions	Embryos excluded from analyses include: 1) Unsuccessfully microinjected embryos that display low or undetectable fluorescence labeling unsuitable for quantitative analysis, and 2) 10-15% of embryos that display arrested or slower development in culture conditions. These exclusion criteria have been utilized in our previous work.
Replication	All experiments in this study were successfully performed at least 3 times with different batches of embryos, mRNA or siRNA preparations.
Randomization	Embryos were randomly allocated into experimental groups. All embryos and cells within embryos were randomly selected for analysis.
Blinding	Successfully developed and imaged embryos have to be selected for subsequent analysis. Therefore, investigators were only blinded for computational analysis following acquisition of imaging data.

## Reporting for specific materials, systems and methods

We require information from authors about some types of materials, experimental systems and methods used in many studies. Here, indicate whether each material, system or method listed is relevant to your study. If you are not sure if a list item applies to your research, read the appropriate section before selecting a response.

### Materials & experimental systems

n/a	Included in the study
<input type="checkbox"/>	<input checked="" type="checkbox"/> Antibodies
<input checked="" type="checkbox"/>	<input type="checkbox"/> Eukaryotic cell lines
<input checked="" type="checkbox"/>	<input type="checkbox"/> Palaeontology
<input type="checkbox"/>	<input checked="" type="checkbox"/> Animals and other organisms
<input checked="" type="checkbox"/>	<input type="checkbox"/> Human research participants
<input checked="" type="checkbox"/>	<input type="checkbox"/> Clinical data

### Methods

n/a	Included in the study
<input checked="" type="checkbox"/>	<input type="checkbox"/> ChIP-seq
<input checked="" type="checkbox"/>	<input type="checkbox"/> Flow cytometry
<input checked="" type="checkbox"/>	<input type="checkbox"/> MRI-based neuroimaging

## Antibodies

### Antibodies used

Primary antibodies:  
 Rat monoclonal anti-Keratin 8 (DSHB, TROMA-I) used at 1:20.  
 Rabbit polyclonal anti-Keratin 18 (Sigma, SAB4501665, Lot #310243) used at 1:200.  
 Mouse monoclonal anti-alpha-tubulin (Sigma, T6199, clone DMIA) used at 1:1000.  
 Rabbit polyclonal anti-alpha-tubulin (GenTex, GTX109832) used at 1:400  
 Rabbit polyclonal anti-Cdx2 (Abcam, 88129) used at 1:200.  
 Mouse monoclonal anti-PLK1 (Thermo Scientific, 37-7000, clone 35-206) used at 1:200  
 Rabbit polyclonal anti-HURP (Atlas antibodies, HPA005546) used at 1:200  
 Mouse monoclonal anti-Polyglutamylated-tubulin (Sigma, T9822, clone B3) used at 1:200  
 Mouse monoclonal anti-Tyrosine tubulin (Sigma, T9028, clone TUB-1A2) used at 1:200  
 Rabbit polyclonal anti-gamma-tubulin (Sigma, T3559) used at 1:500  
 Rat monoclonal anti-E-cadherin (Sigma, U3254, DECMA) used at 1:200

Secondary antibodies:  
 Alexa Fluor 488 Goat anti-Mouse (Invitrogen) used at 1:500.  
 Alexa Fluor 488 Goat anti-Rat (Invitrogen) used at 1:500.  
 Alexa Fluor 488 Goat anti-Rabbit (Invitrogen) used at 1:500.  
 Alexa Fluor 647 Goat anti-Mouse (Invitrogen) used at 1:500.  
 Alexa Fluor 647 Goat anti-Rat (Invitrogen) used at 1:500.  
 Alexa Fluor 647 Goat anti-Rabbit (Invitrogen) used at 1:500.

### Validation

All antibodies were previously validated by vendors and/or published work. Relevant studies include:  
 Keratin 8: filamentous keratin network in ES cells (Schwarz et al. 2015 Sci. Rep. 5: 9007); keratin network in mouse blastocysts showing trophectoderm-specific localization (Ralston and Rossant 2008 Dev. Biol. 313: 614-629).  
 Keratin 18: Validation by manufacturer shows specific filamentous staining of HeLa cells in the presence of the antibody; specific staining in notochordal cells (Rodrigues-Pinto et al. 2016 J Orthop Res 34(8):1327-1340).  
 Alpha-tubulin: Specific localization to interphase and cytokinetic microtubule bridges in mouse embryos (Zenker et al. 2017 Science 357: 925-928); specific localization to mitotic spindles in mouse embryos (Zenker et al. 2018 Cell 173: 776-791).

Cdx2: Specific staining of nuclei in mouse embryos throughout preimplantation development, and elevated levels in trophectoderm cells of the blastocyst relative to those of the inner cell mass (White et al. 2016 Cell 165:75-87); specific staining of nuclei in morula-stage embryos (Samarage et al. 2015 Dev. Cell 34:435-447).  
 PLK1: Staining of spermatocytes (Miyazaki et al. 2017 Genes Cells 22:552-567); arteries (Sur et al. 2016 PLoS One 11:e0147937); gastric samples (Xu et al. 2018 Onco Targets Ther 11:5703-5713); U87 stem cells (Liu et al. 2018 J Cell Mol Med 22:5300-5310).  
 HURP: Specific staining of mitotic spindle (Hsu et al. 2004 J Bio Chem 30;279(31):32592-602).  
 Tyrosine-tubulin: Specific staining of microtubules (Schulte et al. 2010 J Neurosci 14;30(15):5189-203).  
 Gamma-tubulin: Validation of gamma-tubulin siRNA in early mouse embryos (Zenker et al. 2017 Science 357: 925-928)  
 Polyglutamylated-tubulin: Specific localization to hippocampal mouse neuronal culture (Ikegami et al. 2007 PNAS 104(9):3213-8), cilia (Airik et al. 2016 PLoS ONE, 11(5), e0156081-e0156081)  
 E-Cadherin: Blocking of E-cad in mouse embryos (Zenker et al. 2018 Cell, 173(3):776-791.

## Animals and other organisms

Policy information about [studies involving animals](#); [ARRIVE guidelines](#) recommended for reporting animal research

### Laboratory animals

FVB/NTac and HSD:NSA(CF1) wild-type female mice, 4-6 weeks old, were superovulated using 5 iu of pregnant mare serum (PMS, National Hormone and Peptide Program) gonadotropin given intraperitoneally and 5 iu of recombinant chorionic gonadotrophin (CG, National Hormone and Peptide Program) given 48 h after and immediately before mating, according to animal ethics guidelines of the University of Pennsylvania IACUC committee. The animals were housed in the standard BSL2 level animal facility according to the guidelines of UPenn institutional animal care and use committee.

### Wild animals

No wild animals were used.

### Field-collected samples

No field-collected samples were used.

### Ethics oversight

Mouse embryo work was performed according to animal ethics guidelines of the University of Pennsylvania. All protocols were approved by the University of Pennsylvania IACUC committee.

Note that full information on the approval of the study protocol must also be provided in the manuscript.